Thermodynamics of the pyrochlore-lattice quantum Heisenberg antiferromagnet

Patrick Müller,[1] Andre Lohmann,[1] Johannes Richter,[1,2] and Oleg Derzhko[3,2,4]
[1]*Institut für Physik, Otto-von-Guericke-Universität Magdeburg, P.O. Box 4120, 39016 Magdeburg, Germany*
[2]*Max-Planck-Institut für Physik komplexer Systeme, Nöthnitzer Straße 38, 01187 Dresden, Germany*
[3]*Institute for Condensed Matter Physics, National Academy of Sciences of Ukraine, Svientsitskii Street 1, 79011 L'viv, Ukraine*
[4]*Department for Theoretical Physics, Ivan Franko National University of L'viv, Drahomanov Street 12, 79005 L'viv, Ukraine*

(Received 26 January 2019; revised manuscript received 22 June 2019; published 23 July 2019)

We use the rotation-invariant Green's function method (RGM) and the high-temperature expansion to study the thermodynamic properties of the Heisenberg antiferromagnet on the pyrochlore lattice. We discuss the excitation spectra as well as various thermodynamic quantities, such as spin correlations, uniform susceptibility, specific heat, and static and dynamical structure factors. For the ground state we present RGM data for arbitrary spin quantum numbers S. At finite temperatures we focus on the extreme quantum cases $S = \frac{1}{2}$ and 1. We do not find indications for magnetic long-range order for any value of S. We discuss the width of the pinch point in the static structure factor in dependence on temperature and spin quantum number. We compare our data with experimental results for the pyrochlore compound $NaCaNi_2F_7$ ($S = 1$). Thus, our results for the dynamical structure factor agree well with the experimentally observed features at 3 ...8 meV for $NaCaNi_2F_7$. We analyze the static structure factor $S_{\mathbf{q}}$ to find regions of maximal $S_{\mathbf{q}}$. The high-temperature series of the $S_{\mathbf{q}}$ provide a fingerprint of weak *order by disorder* selection of a collinear spin structure, where (classically) the total spin vanishes on each tetrahedron and neighboring tetrahedra are dephased by π.

DOI: 10.1103/PhysRevB.100.024424

I. INTRODUCTION

Geometrically frustrated magnetic materials are a subject of great interest nowadays. Phenomena of geometric frustration may emerge if nearest-neighbor antiferromagnetic interactions occur in periodic lattices based on triangles as elementary objects of the lattice structure since the spins within a triangular cell cannot be mutually antiparallel. One of the most prominent spin models in the field of geometrically frustrated magnetism is the pyrochlore Heisenberg antiferromagnet (PHAF). The pyrochlore lattice is a three-dimensional arrangement of corner-sharing tetrahedra (see Fig. 1). There are several families of compounds in nature with magnetic atoms which reside on the pyrochlore-lattice sites and interact with their neighbors through antiferromagnetic exchange interactions (see, e.g., Refs. [1–3]). On the other hand, this spin model presents a playground for the study of geometric frustration in three dimensions. It is highly nontrivial and is far from being fully understood. Even in the classical limit there is no magnetic order and the ground state is a classical spin liquid with algebraically decaying spin-spin correlations [4,5]. For low spin quantum numbers S the complexity of the model increases since quantum fluctuations become important. Thus, so far for the quantum model no accurate values for the ground-state energy are available. At finite temperatures, the interplay of quantum and thermal fluctuations makes a theoretical investigation even more challenging. While for the classical PHAF several accurate numerical tools are available (e.g., Monte Carlo and molecular dynamics), such straightforward numerical tools do not work for the quantum PHAF.

Let us mention here two other models, which will be used below to compare with the PHAF, namely, the Heisenberg antiferromagnet (HAFM) on the simple-cubic lattice and on the kagome lattice. The former one, that orders below the Néel temperature $T_N > 0$, can be considered as the unfrustrated counterpart of the PHAF since the simple-cubic lattice has also six nearest neighbors. The latter one, that does not order in the ground state for low spin quantum number, can be considered as the two-dimensional analog of the PHAF.

Most of the previous studies on the quantum PHAF were focused on the ground-state properties of the model. Thus, a field-theory attempt to understand the nature of the ground state was reported in Ref. [6]. The bond-operator-method calculations of Ref. [7] leads to a valence-bond-crystal state as the ground state of the model. Perturbative expansions starting from noninteracting tetrahedral unit cells which yield the spin correlations for the model were performed in Refs. [8,9]. The conclusion of this study is that the ground state is a spin liquid with exponentially decaying correlations, where the correlation length does not exceed the nearest-neighbor distance. Similar approaches starting from the limit of isolated tetrahedra and switching on the interactions between the tetrahedra as perturbation were later on presented in Refs. [10–13]. The contractor renormalization method applied to the spin-$\frac{1}{2}$ PHAF leads to the conclusion that the ground state is a valence bond solid breaking lattice symmetry [14]. Other routes to the problem, which do not start from less symmetric Hamiltonians to be treated perturbatively, were considered in Refs. [15,16]. In these papers, the spin-$\frac{1}{2}$ problem on the pyrochlore lattice was studied after enlarging the symmetry of the spin space from SU(2) $\sim$ Sp(1) to Sp(N) [15,16], however, the large-N physics cannot be uniquely transferred to SU(2) $\sim$ Sp($N = 1$) limit. Fermionic mean-field theory followed by variational Monte Carlo [17] as well

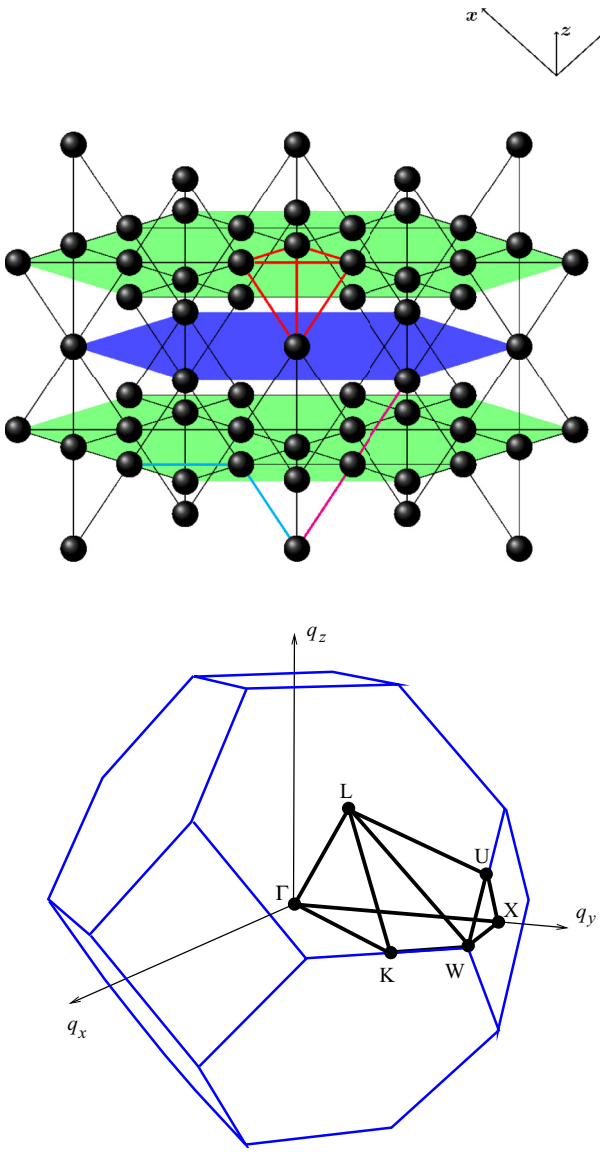

FIG. 1. (Top) The pyrochlore lattice visualized here as a three-dimensional structure which consists of alternating kagome (green) and triangular (blue) planar layers. The four-site unit cell is marked with the red bonds. A red bond also indicates the nearest-neighbor correlation function c_{100}. The path which connects the two sites entering the correlation function c_{110} (c_{200}) is colored in cyan (violet) (see the main text). (Bottom) The first Brillouin zone of a face-centered-cubic Bravais lattice. The points Γ, X, W, K, U, and L in the $\mathbf{q}$ space are given by $\Gamma = (0, 0, 0)$, $\mathrm{X} = (0, 2\pi, 0)$, $\mathrm{W} = (\pi, 2\pi, 0)$, $\mathrm{K} = (3\pi/2, 3\pi/2, 0)$, $\mathrm{U} = (\pi/2, 2\pi, \pi/2)$, and $\mathrm{L} = (\pi, \pi, \pi)$ (see, e.g., Refs. [18,31]).

as a large-N SU(N) fermionic mean-field theory [18] suggested a chiral spin-liquid state as the ground state of the $S = \frac{1}{2}$ PHAF. Large-S approaches for the PHAF were discussed in Refs. [19–21]. They yield indications that via the *order by disorder mechanism* quantum fluctuations select collinear states among the huge degenerate manifold of classical ground states. We may mention here the difference to the kagome HAFM, where collinear states are not present in the classical ground-state manifold.

Among very recent papers on the quantum PHAF we may mention an analytical study (a flavor-wave theory combined with a mean-field approach) of a $S = 1$ model with Dzyaloshinskii-Moriya interaction and single-ion spin anisotropy [22], exact-diagonalization calculations for a $S = \frac{1}{2}$ system of up to 36 sites [23], or investigations of low-temperature phases of the quantum spin-S PHAF including nearest-neighbor and next-nearest-neighbor interactions using the pseudofermion functional renormalization group method (PFFRG) [24]. The dynamical structure factor of the $S = 1$ pyrochlore material $NaCaNi_2F_7$ has been studied with a combination of molecular dynamics simulations, stochastic dynamical theory, and linear spin-wave theory [25].

So far, less attention has been paid to finite-temperature properties. We have to mention here the studies on the checkerboard lattice (planar pyrochlore) and pyrochlorelike models of the mineral clinoatacamite using numerical linked-cluster expansions along with exact diagonalization of finite clusters [26,27]. Furthermore, the diagrammatic Monte Carlo simulations for correlation functions down to the temperature $J/6$ were performed in Ref. [28]. They reveal spin-ice states at $T = J/6$ although the lower temperatures remain inaccessible [28]. The above-mentioned study [24] of the spin-S J_1-J_2 Heisenberg model on the pyrochlore lattice employing the PFFRG includes both the ground-state and thermodynamic properties. The theoretical study on the $S = 1$ pyrochlore material $NaCaNi_2F_7$ [25] also refers to finite (although low) temperatures. In what follows, we shall come back to some of these results.

The goal of this study is to describe the properties of the quantum PHAF at arbitrary temperatures, including low, intermediate, and high temperatures. In addition, we also present data for the ground-state energy, the uniform susceptibility, the excitation spectrum, the spin-spin correlation functions, and structure factors at zero temperature. The toolbox to study finite-temperature properties of the highly frustrated three-dimensional spin model is sparse. Here, we use two universal methods, a second-order rotation-invariant Green's function method (RGM) [29] and a high-temperature expansion (HTE) [30]. While the HTE is restricted to temperatures above $\sim J$, the RGM is applicable for arbitrary temperatures.

The rest of the paper is organized as follows. In Sec. II we briefly introduce the PHAF model and then in Sec. III we describe concisely the methods used for calculations. We discuss our findings for the PHAF in Secs. IV (zero-temperature results) and V (finite-temperature results). Finally, in Sec. VI we summarize our work. The Appendix contains lengthy formulas for a few high-temperature-expansion terms for the static structure factor of the PHAF with $S = \frac{1}{2}$, 1, and $\frac{3}{2}$.

II. MODEL

We consider the Heisenberg model on the pyrochlore lattice (see Fig. 1, top) given by

$$\hat{H} = J \sum_{\langle m\alpha, n\beta \rangle} \hat{\mathbf{S}}_{m\alpha} \cdot \hat{\mathbf{S}}_{n\beta}. \tag{2.1}$$

The sum in Eq. (2.1) runs over all nearest-neighbor bonds. The antiferromagnetic nearest-neighbor coupling is set to

unity, $J = 1$, and $\hat{\mathbf{S}}^2_{m\alpha} = S(S+1)$, $S \geqslant \frac{1}{2}$. The pyrochlore lattice is described as four interpenetrating face-centered-cubic sublattices. The origins of these sublattices are taken to be $\mathbf{r}_1 = (0,0,0)$, $\mathbf{r}_2 = (0, \frac{1}{4}, \frac{1}{4})$, $\mathbf{r}_3 = (1/4, 0, 1/4)$, and $\mathbf{r}_4 = (\frac{1}{4}, \frac{1}{4}, 0)$, whereas the sites of the face-centered-cubic lattice are determined by $\mathbf{R}_m = m_1\mathbf{e}_1 + m_2\mathbf{e}_2 + m_3\mathbf{e}_3$, where m_1, m_2, m_3 are integers and $\mathbf{e}_1 = (0, 1/2, 1/2)$, $\mathbf{e}_2 = (\frac{1}{2}, 0, \frac{1}{2})$, $\mathbf{e}_3 = (\frac{1}{2}, \frac{1}{2}, 0)$. As a result, the N pyrochlore-lattice sites are labeled by $m\alpha$, $\mathbf{R}_{m\alpha} = \mathbf{R}_m + \mathbf{r}_\alpha$, where $m = 1, \ldots, \mathcal{N}$, $\mathcal{N} = N/4$ is the number of unit cells, and $\alpha = 1, 2, 3, 4$ labels the sites in the unit cell. The nearest-neighbor separation is $d = \sqrt{2}/4 \approx 0.35$. In Fig. 1 (bottom) we also show the first Brillouin zone of a face-centered-cubic Bravais lattice along with some symmetric points in the $\mathbf{q}$ space to be used in what follows.

The pyrochlore-lattice Heisenberg Hamiltonian (2.1) can be rewritten through a sum over $N/2$ tetrahedra [32–34]: $2\hat{H}/J = \sum_{T=1}^{N/2} \hat{\mathbf{S}}^2_T - \sum_{T=1}^{N/2}\sum_{\alpha=1}^{4} \hat{\mathbf{S}}^2_{T\alpha}$, where $\hat{\mathbf{S}}_T = \hat{\mathbf{S}}_{T1} + \hat{\mathbf{S}}_{T2} + \hat{\mathbf{S}}_{T3} + \hat{\mathbf{S}}_{T4}$ is the total spin of the tetrahedron T and $\hat{\mathbf{S}}^2_{T\alpha} = S(S+1)$. In the classical limit $S \to \infty$, when all $\hat{\mathbf{S}}^2_T$ commute, the ground-state configurations are given by the constraint $\hat{\mathbf{S}}^2_T = 0$ on each tetrahedron separately. This results in a massive ground-state degeneracy, although the ground-state energy per site is quite simple and is given by $E_0/N = -S^2J$.

From the experimental side, there are only a few compounds which can be described by the model (2.1). In addition to the already mentioned fluoride $NaCaNi_2F_7$ which provides a good realization of the $S = 1$ PHAF, there are compounds which at least in their high-temperature phases are candidates for the PHAF (2.1). For example, the molybdate $Y_2Mo_2O_7$ (which, however, shows spin-glass behavior at low temperature and spin-orbit coupling is relevant) [35–37], the chromites ACr_2O_4 (A = Mg,Zn,Cd) (which, however, show a magneto-structural transition at low temperatures) [38–40], or FeF_3 (for which aside from the nearest-neighbor antiferromagnetic Heisenberg interaction, also biquadratic and Dzyaloshinskii-Moriya interactions are present) [41].

III. METHODS

A. Rotation-invariant Green's function method (RGM)

Our first method used in this study of the PHAF is a double-time temperature-dependent Green's function technique which is widely employed in quantum many-body theory [42–44]. An important development of this approach was achieved by Kondo and Yamaji [29] by introducing a rotation-invariant formalism to describe short-range order of the one-dimensional $S = \frac{1}{2}$ Heisenberg ferromagnet at $T > 0$. Going one step beyond the usual random-phase approximation (Tyablikov approximation) [42–45] the rotational invariance is introduced by setting $\langle \hat{S}^z_i \rangle = 0$ in the equations of motion. Within this scheme, possible magnetic long-range order is described by the long-range term (condensation part) in the spin-spin correlation function (see, e.g., Refs. [46–49]). Moreover, the decoupling approximation of higher-order correlators is improved by introducing so-called vertex parameters (see below). We mention here that the first-order random-phase approximation fails for the PHAF since it is not appropriate to describe magnetic phases with short-range order [29,47, 50–52].

Since 1972 the rotation-invariant Green's function method (RGM) was continuously further developed and nowadays it is a well-established technique that has been used in numerous recent studies on quantum spin systems (including arbitrary quantum spin number S, any lattice dimension, lattices with nonprimitive unit cell, geometrically frustrated lattices) [48–66].

To be more specific, in this study of the PHAF we deal with a set of Green's functions $\langle\langle \hat{S}^\mu_{\mathbf{q}\alpha}; \hat{S}^\nu_{\mathbf{q}\beta} \rangle\rangle_\omega = -\chi^{\mu\nu}_{\mathbf{q}\alpha\beta}(\omega)$, where $\langle\langle \hat{A}; \hat{B} \rangle\rangle_t = -i\Theta(t)\langle [\hat{A}(t), \hat{B}]_- \rangle$, the subscript ω means the Fourier transform with respect to the time t, $\mu\nu$ denotes $+-$ or zz, and $\hat{S}^+_{\mathbf{q}\alpha} = \sum_m \exp(-i\mathbf{q}\cdot\mathbf{R}_m)\hat{S}^+_{m\alpha}/\sqrt{\mathcal{N}}$ (the sum runs over all unit cells, i.e., $m = 1, \ldots, \mathcal{N}$). Moreover, the dynamical susceptibilities $\chi^{\mu\nu}_{\mathbf{q}\alpha\beta}(\omega)$ are immediately known once the Green's functions are determined.

In Ref. [52] it was shown that within the framework of the RGM the equations of motion can be compactly written in the following matrix form:

$$(\omega^2 I - F_{\mathbf{q}})\chi^{+-}_{\mathbf{q}}(\omega) = -M_{\mathbf{q}}. \tag{3.1}$$

Since the unit cells contain four sites, the matrices in Eq. (3.1) are 4×4 Hermitian matrices, namely, the unit matrix I, the frequency matrix $F_{\mathbf{q}}$, the susceptibility matrix $\chi^{+-}_{\mathbf{q}}(\omega)$, and the moment matrix $M_{\mathbf{q}}$. Although the study of Ref. [52] concerns the spin-S ferromagnetic case, the RGM equations derived there hold for the antiferromagnetic coupling $J = 1$, too, because they do not depend on the sign of the exchange interaction. [For explicit expressions for the moment matrix and the frequency matrix, see Eqs. (5) and (6) in Ref. [52]]. Importantly, these matrix elements contain spin correlation functions $c_{ijk} \equiv \langle \hat{S}^+_{\mathbf{0}} \hat{S}^-_{\mathbf{R}} \rangle$, $\mathbf{R} = i\mathbf{r}_2 + j\mathbf{r}_3 + k\mathbf{r}_4$. Due to lattice symmetry, only the nonequivalent correlators c_{100}, c_{110}, and c_{200} enter the matrix elements, where c_{100} is related to the sites connected by the edge of unit-cell tetrahedron (nearest-neighbor correlator), c_{110} is related to the sites of two adjacent unit-cell tetrahedra connected by two noncollinear edges with a common site (next-nearest-neighbor correlator), and c_{200} is related to the sites of two adjacent unit-cell tetrahedra connected by two collinear edges with a common site (one of the two kinds of third-neighbor correlators) (see Fig. 1, top). These correlators appear in the matrix elements through $\tilde{\alpha}_{ijk} = \alpha_{ijk}c_{ijk}$ and $\tilde{\lambda}_{ijk} = \lambda_{ijk}c_{ijk}$. Here α_{ijk} and λ_{ijk} are the vertex parameters which are introduced to improve the approximation made by the decoupling in second order, e.g., $\hat{S}^+_A\hat{S}^-_B\hat{S}^z_C \to \alpha_{AB}c^{+-}_{AB}\hat{S}^z_C$ or $\hat{S}^+_A\hat{S}^-_B\hat{S}^z_B \to \lambda_{AB}c^{+-}_{AB}\hat{S}^z_B$. Moreover, we have $\lambda_{ijk} = 0$ for $S = \frac{1}{2}$.

Going back to Eq. (3.1), it is important to note that the moment matrix $M_{\mathbf{q}}$ and the frequency matrix $F_{\mathbf{q}}$ commute, i.e., $[M_{\mathbf{q}}, F_{\mathbf{q}}]_- = 0$. Let us denote the common eigenvectors of the matrices $M_{\mathbf{q}}$ and $F_{\mathbf{q}}$ by $|\gamma\mathbf{q}\rangle$, $\gamma = 1, 2, 3, 4$. Moreover, let us introduce their eigenvalues, i.e., $M_{\mathbf{q}}|\gamma\mathbf{q}\rangle = m_{\gamma\mathbf{q}}|\gamma\mathbf{q}\rangle$ and $F_{\mathbf{q}}|\gamma\mathbf{q}\rangle = \omega^2_{\gamma\mathbf{q}}|\gamma\mathbf{q}\rangle$. In Ref. [52] it has been found that

$$\frac{m_{1\mathbf{q}}}{J} = \frac{m_{2\mathbf{q}}}{J} = \frac{m_{3\mathbf{q}}}{J} + \frac{m_{4\mathbf{q}}}{J} = -16c_{100},$$
$$\frac{m_{3\mathbf{q}}}{J} - \frac{m_{4\mathbf{q}}}{J} = -8c_{100}D_{\mathbf{q}} \tag{3.2}$$

with $D_{\mathbf{q}}^2 = 1 + \cos(q_x/2)\cos(q_y/2) + \cos(q_x/2)\cos(q_z/2) + \cos(q_y/2)\cos(q_z/2)$ and

$$\begin{aligned}
\frac{\omega_{1\mathbf{q}}^2}{J^2} = \frac{\omega_{2\mathbf{q}}^2}{J^2} &= \frac{8}{3}[2S(S+1) + 3\tilde{\lambda}_{100} \\
&\quad + 9\tilde{\alpha}_{100} + 6\tilde{\alpha}_{110} + 3\tilde{\alpha}_{200}], \\
\frac{\omega_{3\mathbf{q}}^2}{J^2} + \frac{\omega_{4\mathbf{q}}^2}{J^2} &= \frac{8}{3}\big[2S(S+1) + 3\tilde{\lambda}_{100} \\
&\quad + 3\big(D_{\mathbf{q}}^2 - 1\big)\tilde{\alpha}_{100} + 6\tilde{\alpha}_{110} + 3\tilde{\alpha}_{200}\big], \\
\frac{\omega_{3\mathbf{q}}^2}{J^2} - \frac{\omega_{4\mathbf{q}}^2}{J^2} &= \frac{8}{3}D_{\mathbf{q}}S(S+1) \\
&\quad + 4D_{\mathbf{q}}(\tilde{\lambda}_{100} + 3\tilde{\alpha}_{100} + 2\tilde{\alpha}_{110} + \tilde{\alpha}_{200}). \qquad (3.3)
\end{aligned}$$

The common eigenvectors $|\gamma\mathbf{q}\rangle$ of the moment matrix $M_{\mathbf{q}}$ and the frequency matrix $F_{\mathbf{q}}$ are rather lengthy; they are presented in Appendix B in Ref. [52].

Now we can resolve Eq. (3.1) to find the set of dynamical susceptibilities (Green's functions). They are given by

$$\chi_{\mathbf{q}\alpha\beta}^{+-}(\omega) = -\sum_{\gamma} \frac{m_{\gamma\mathbf{q}}}{\omega^2 - \omega_{\gamma\mathbf{q}}^2}\langle\alpha|\gamma\mathbf{q}\rangle\langle\gamma\mathbf{q}|\beta\rangle, \qquad (3.4)$$

where $\langle\alpha|\gamma\mathbf{q}\rangle$ is the αth component of the eigenvector $|\gamma\mathbf{q}\rangle$. The correlation functions are obtained by applying the spectral theorem

$$\begin{aligned}
c_{m\alpha,n\beta} &= \frac{1}{\mathcal{N}}\sum_{\mathbf{q}\neq\mathbf{Q}} c_{\mathbf{q}\alpha\beta}\cos(\mathbf{q}\cdot\mathbf{r}_{m\alpha,n\beta}) \\
&\quad + \sum_{\mathbf{Q}} C_{\mathbf{Q}\alpha\beta}\cos(\mathbf{Q}\cdot\mathbf{r}_{m\alpha,n\beta}) \qquad (3.5)
\end{aligned}$$

with

$$c_{\mathbf{q}\alpha\beta} = \sum_{\gamma}\frac{m_{\gamma\mathbf{q}}}{2\omega_{\gamma\mathbf{q}}}[1 + 2n(\omega_{\gamma\mathbf{q}})]\langle\alpha|\gamma\mathbf{q}\rangle\langle\gamma\mathbf{q}|\beta\rangle, \qquad (3.6)$$

where $n(\omega) = 1/[\exp(\omega/T) - 1]$ is the Bose-Einstein distribution function and $C_{\mathbf{Q}\alpha\beta}$ is the so-called condensation term which is related to magnetic long-range order (see, e.g., Refs. [46–49]). For example, for the ferromagnet [52], only one condensation term at $\mathbf{Q} = \mathbf{0}$ is relevant, i.e., $C_{\mathbf{0}\alpha\beta} = C_{\mathbf{0}}$, and the total magnetization is given by the expression $M = \sqrt{3C_{\mathbf{0}}/2}$. The susceptibility $\chi_{\mathbf{Q}}$ is given by the expression

$$\begin{aligned}
\chi_{\mathbf{Q}} \equiv \chi_{\mathbf{Q}}^{zz} = \chi_{\mathbf{Q}}^{+-}/2 &= \lim_{(\mathbf{q},\omega)\to(\mathbf{Q},0)}\frac{1}{4}\sum_{\alpha}\sum_{\beta}\frac{\chi_{\mathbf{q}\alpha\beta}^{+-}(\omega)}{2} \\
&= \lim_{\mathbf{q}\to\mathbf{Q}}\sum_{\alpha,\beta,\gamma}\frac{m_{\gamma\mathbf{q}}}{8\omega_{\gamma\mathbf{q}}^2}\langle\alpha|\gamma\mathbf{q}\rangle\langle\gamma\mathbf{q}|\beta\rangle. \qquad (3.7)
\end{aligned}$$

In case of magnetic long-range order, $\chi_{\mathbf{Q}}$ diverges at a critical temperature T_c, where $\mathbf{Q}$ is the magnetic wave vector. According to Eq. (3.7), this would be related to divergence of $m_{\gamma\mathbf{q}}/\omega_{\gamma\mathbf{q}}^2$ as $\mathbf{q}\to\mathbf{Q}$. For the further discussion of the relevant RGM equations it is important to state here, that within the RGM for the PHAF we do not find such a divergence for all $\mathbf{Q}$ and all temperatures $T \geqslant 0$. This means that for the PHAF there is no condensation term or, in other words, no magnetic long-range order for all temperatures $T \geqslant 0$.

Knowing the dynamical susceptibilities or the Green's functions (3.4) and the correlation functions (3.5) and (3.6), we can easily obtain the (zero-frequency) susceptibility $\chi_{\mathbf{Q}}$ [Eq. (3.7)] and the specific heat C_V. Furthermore, using Eq. (3.6) we can also obtain the static structure factor $S_{\mathbf{q}} = 3S_{\mathbf{q}}^{+-}/2$, $S_{\mathbf{q}}^{+-} = \sum_{\alpha,\beta} c_{\mathbf{q}\alpha\beta}/4$. Last but not least, the dynamical structure factor $S_{\mathbf{q}}^{zz}(\omega) = S_{\mathbf{q}}^{+-}(\omega)/2$ follows from the fluctuation-dissipation theorem, i.e., $S_{\mathbf{q}}^{+-}(\omega) = [2/(1 - e^{-\omega/T})]\mathrm{Im}\chi_{\mathbf{q}}^{+-}(\omega)$, $\chi_{\mathbf{q}}^{+-}(\omega) = \sum_{\alpha,\beta}\chi_{\mathbf{q}\alpha\beta}^{+-}(\omega)/4$. Thus, Eq. (3.4) leads straightforwardly to $S_{\mathbf{q}}^{+-}(\omega)$. After some standard manipulations we arrive at

$$\begin{aligned}
S_{\mathbf{q}}^{zz}(\omega) &= \frac{\pi}{1 - e^{-\frac{\omega}{T}}}\sum_{\alpha,\beta}\sum_{\gamma}\frac{m_{\gamma\mathbf{q}}}{8\omega_{\gamma\mathbf{q}}} \\
&\quad \times [\delta(\omega - \omega_{\gamma\mathbf{q}}) - \delta(\omega + \omega_{\gamma\mathbf{q}})]\langle\alpha|\gamma\mathbf{q}\rangle\langle\gamma\mathbf{q}|\beta\rangle. \qquad (3.8)
\end{aligned}$$

This quantity is related to neutron inelastic scattering data accessible in experiments. We also note that integrating $S_{\mathbf{q}}^{zz}(\omega)$ [Eq. (3.8)] over all ω we get the static structure factor:

$$\int_{-\infty}^{\infty} d\omega\, S_{\mathbf{q}}^{zz}(\omega) = 2\pi S_{\mathbf{q}}^{zz} = 2\pi\frac{1}{3}S_{\mathbf{q}}. \qquad (3.9)$$

Note that there is no intrinsic damping within the RGM approach. Therefore, we replace the δ functions in Eq. (3.8) by the Lorentzian function, i.e., $\delta(x) \to (1/\pi)[\epsilon/(x^2 + \epsilon^2)]$, where the "damping" parameter ϵ is chosen as $\epsilon = 0.1$.

In summary, for the considered antiferromagnetic case, i.e., $J = 1$, we have to solve self-consistently the equations for the correlation functions c_{100}, c_{110}, c_{200}, and the vertex parameters. Taking into account all possible vertex parameters $\alpha_{ijk}(T)$ and $\lambda_{ijk}(T)$ would therefore exceed the number of available equations. In the simplest version of the RGM, often called the minimal version, one considers only one vertex parameter in each class, i.e., $\alpha_{ijk}(T) = \alpha(T)$ and $\lambda_{ijk}(T) = \lambda(T)$. We mention that this simple version with only one α parameter was used in the early RGM kagome papers for the $S = \frac{1}{2}$ case [where $\lambda(T) \equiv 0$] [53–55]. An improvement of the minimal version can be achieved by taking into account more vertex parameters, however, that requires additional input to get more equations for the additional vertex parameters. For example, in Ref. [66], for the kagome-lattice spin-S HAFM, two α parameters (α_1 for nearest-neighbor sites and α_2 for not-nearest-neighbor sites) are introduced and the value of the ground-state energy obtained by the coupled cluster method (CCM) [67] is used as an additional input. In the case of the quantum PHAF we do not have such data, and, therefore, we have to restrict ourselves to the minimal version of the RGM. In Ref. [66], by comparison of the minimal and the extended version using the CCM input, it has been found that for the kagome HAFM the minimal version works reasonably well for small spin quantum numbers S, but may fail for large S.

Within the minimal version, the set of equations is found as follows. For every unknown correlation function the spectral theorem yields one equation. One more equation is given by the sum rule $\hat{\mathbf{S}}_{m\alpha}^2 = S(S+1)$, which determines, e.g., one vertex parameter. Thus, for $S = \frac{1}{2}$, where $\lambda = 0$, these equations determine all unknown quantities. For $S > \frac{1}{2}$, additionally

the unknown parameter λ has to be determined. For that we follow Refs. [50,52,63–66]. At zero temperature we use the well-tested ansatz $\lambda(0) = 2 - 1/S$. At infinite temperature $\lambda(\infty) = 1 - 3/[4S(S+1)]$ is valid, as it has been verified by comparison with the high-temperature expansion. For intermediate temperatures we set the ratio

$$r(T) \equiv \frac{\lambda(T) - \lambda(\infty)}{\alpha(T) - \alpha(\infty)} = \frac{\lambda(0) - \lambda(\infty)}{\alpha(0) - \alpha(\infty)} \tag{3.10}$$

as temperature independent.

B. High-temperature expansion (HTE)

Our second method used in this study of the PHAF is the high-temperature expansion (HTE) which is a universal and straightforward approach in the theory of spin systems [30]. To be more specific, in this study we use the HTE program of Ref. [68], which is freely available at [69], in an extended version up to 13th (11th) order for $S = \frac{1}{2}$ ($S > \frac{1}{2}$). With this tool, we compute the series of the static uniform susceptibility $\chi_0 = \sum_n c_n \beta^n$ and the specific heat $C_V = \sum_n d_n \beta^n$ with respect to the inverse temperature $\beta = 1/T$. To extend the region of validity of the power series we use Padé approximants denoted by $[m, n] = P_m(\beta)/Q_n(\beta)$, where $P_m(\beta)$ and $Q_n(\beta)$ are polynomials in β of order m and n, respectively. The coefficients of $P_m(\beta)$ and $Q_n(\beta)$ are determined by the condition that the expansion of $[m, n]$ has to agree with the initial power series up to order $O(\beta^{m+n})$.

In addition, the high-temperature series of the static spin pair correlation function $\langle \hat{\mathbf{S}}_i \cdot \hat{\mathbf{S}}_j \rangle$ are calculated up to 12th order of β (for $S = \frac{1}{2}$) or 10th order of β (for $S > \frac{1}{2}$), following the strategy of Refs. [68,70]. Having the series of the correlation functions we evaluate the magnetic static structure factor

$$S_{\mathbf{q}} = \frac{1}{N} \sum_{i,j} \langle \hat{\mathbf{S}}_i \cdot \hat{\mathbf{S}}_j \rangle \cos\left(\mathbf{q} \cdot (\mathbf{R}_i - \mathbf{R}_j)\right) \tag{3.11}$$

(see, e.g., Ref. [66]). Here, i and j are the sites of the pyrochlore lattice labeled in Sec. II by $m\alpha$. Evidently, $S_{\mathbf{q}} = 3S^{+-}_{\mathbf{q}}/2$.

IV. ZERO-TEMPERATURE PROPERTIES

We begin this section with a discussion of the quality of the minimal-version RGM for the PHAF. As briefly explained in Sec. III A, the minimal version neglects the real-space dependence of the α parameter and is believed to be justified preferably for ferromagnets. To estimate the accuracy of the adopted scheme for the PHAF we follow Ref. [66] and consider the RGM ground-state energy as well as the ground-state uniform susceptibility χ_0 as a function of $1/S$ (see Fig. 2). It is obvious that in the classical limit $S \to \infty$ we obtain the correct result for the ground-state energy $E_0 = -NS^2J$ [32] (Fig. 2, top). Note that this is contrary to the case of the kagome-lattice HAFM, where the minimal version in the classical limit $S \to \infty$ gives a higher energy value than the exact one and the discrepancy was removed after adopting the extended version [66]. The ground-state energies per site for the pure quantum case of $S = \frac{1}{2}$ obtained by other approaches

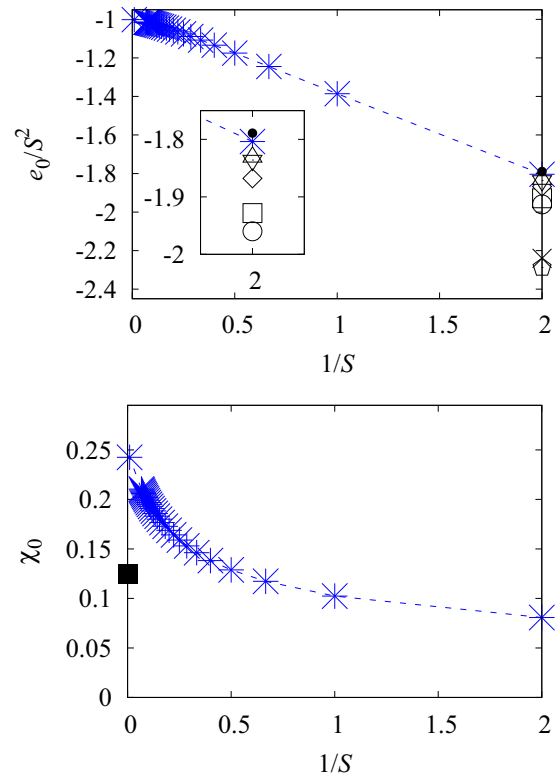

FIG. 2. RGM results (blue symbols) for the ground-state energy $E_0/(NS^2)$ (top) and the ground-state uniform susceptibility χ_0 (bottom) of the PHAF ($J = 1$) as a function of the inverse spin-quantum number $1/S$. The black symbols in the upper panel correspond to the results of Ref. [18] (filled circles), Refs. [6,10] (open circles), Ref. [71] (pentagons), Ref. [7] (up triangles), Ref. [9] (crosses), Ref. [17] (down triangles); squares and diamonds correspond to exact-diagonalization data for $N = 28$ and 36, respectively [23]. The inset contains some data for $S = \frac{1}{2}$ using an enlarged scale. The black square in the lower panel corresponds to the result of classical Monte Carlo simulations [72].

exhibit a pretty wide distribution (see the black symbols in Fig. 2, top) ranging from $e_0 \approx -0.572J$ [71] to $e_0 \approx -0.447J$ [18], thus providing evidence that reliable values in this limit are still lacking. The ground-state uniform susceptibility χ_0 is shown in the lower panel of Fig. 2. As a function of the inverse spin-quantum number χ_0 exhibits a noticeable upturn for $S \gtrsim 2$ leading finally to a significant deviation from classical Monte Carlo result $\chi_0 \approx 0.125$ [72–74]. Note here that the kagome HAFM exhibits an unphysical divergence of the ground-state value of χ_0 as $S \to \infty$ when using the minimal version of the RGM [66]. Thus, we may conclude that the minimal version of the RGM likely works reasonably well for the ground state of the PHAF, however, for increasing S the RGM data become less reliable. Moreover, in what follows we report results at $T = 0$, low, intermediate, and high temperatures and compare them with the outcomes of other approaches. We believe that the investigation of this highly complex and challenging spin model by various techniques is a reasonable route to shed more light upon the PHAF.

We turn to the discussion of the ground-state excitation spectrum for the PHAF. We start with a brief discussion of

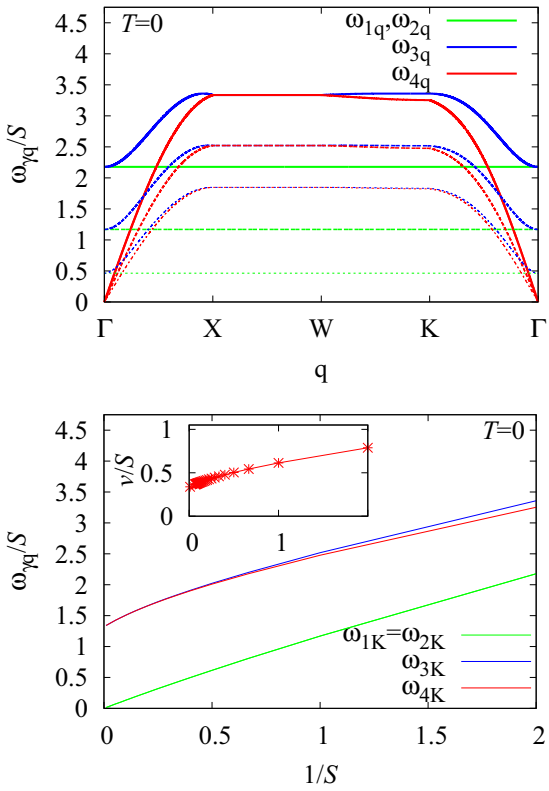

FIG. 3. (Top) Dispersion of the excitation energies $\omega_{\gamma\mathbf{q}}/S$ [Eq. (3.3)], $J = 1$] at zero temperature $T = 0$ for $S = \frac{1}{2}$ (thick), $S = 1$ (thin), and $S = 3$ (very thin). The points Γ, X, W, and K in the first Brillouin zone of a face-centered-cubic Bravais lattice are given by $\Gamma = (0, 0, 0)$, $\mathrm{X} = (0, 2\pi, 0)$, $\mathrm{W} = (\pi, 2\pi, 0)$, and $\mathrm{K} = (3\pi/2, 3\pi/2, 0)$ (see Fig. 1, bottom). (Bottom, main panel) The ground-state excitation energies $\omega_{\gamma\mathbf{q}}/S$ in dependence on the inverse spin-quantum number $1/S$ at $\mathbf{q} = (3\pi/2, 3\pi/2, 0)$ (K point). (Bottom, inset) Normalized RGM ground-state excitation velocity v/S in dependence on $1/S$.

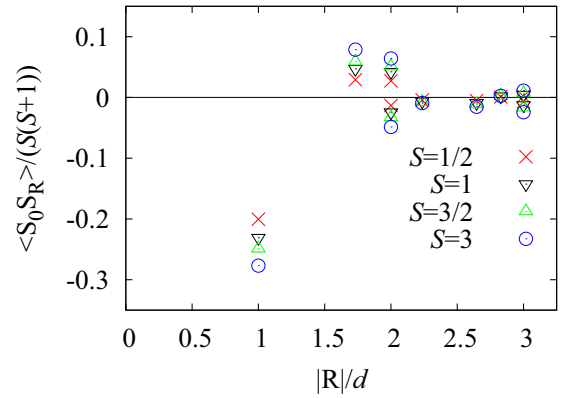

FIG. 4. Ground-state correlation functions $\langle\hat{\mathbf{S}}_\mathbf{0}\cdot\hat{\mathbf{S}}_\mathbf{R}\rangle/[S(S+1)]$ within a range of separation $|\mathbf{R}|/d \leqslant 3$, where $d = \sqrt{2}/4 \approx 0.35$ is the nearest-neighbor separation, $c_{100} < 0$ ($R = d = \sqrt{2}/4 \approx 0.35$), $c_{110} > 0$ ($R = \sqrt{6}/4 \approx 0.61$), $c_{200} > 0$ ($R = \sqrt{2}/2 \approx 0.71$), $c_{2\text{-}20} < 0$ ($R = \sqrt{2}/2 \approx 0.71$), $c_{21\text{-}1} < 0$ ($R = \sqrt{10}/4 \approx 0.79$), $c_{210} < 0$ ($R = \sqrt{14}/4 \approx 0.94$), $c_{22\text{-}2} > 0$ ($R = 1$), $c_{300} < 0$ ($R = 3\sqrt{2}/4 \approx 1.06$), and $c_{3\text{-}30} > 0$ ($R = 3\sqrt{2}/4 \approx 1.06$), for the quantum PHAF obtained within the minimal-version RGM for $S = \frac{1}{2}$ (crosses), $S = 1$ (down triangles), $S = \frac{3}{2}$ (up triangles), and $S = 3$ (circles). Note that for several separations R inequivalent correlators exist.

the linear-spin-wave spectrum [71]. The starting point of the linear spin-wave theory is a classical ground state. In the case of the PHAF the classical ground state has a huge degeneracy. The selection of the classical ground state for linear spin-wave theory is then guided by some physical intuition and might be biased. In Ref. [71], several classical ordered ground states with identical magnetic and crystallographic unit cells were considered (so-called $\mathbf{q} = \mathbf{0}$ states). In all considered cases, the linear-spin-wave spectrum contains flat zero energy as well as dispersive modes. In particular, for the collinear classical state there are two degenerate flat zero-energy modes and two degenerate dispersive modes; for the noncollinear ground state, where the spins point along the diagonals of the tetrahedron, all four modes are different and the lowest one is the flat zero-energy mode.

The RGM data for the excitation spectrum $S = \frac{1}{2}$ (thick), $S = 1$ (thin), and $S = 3$ (very thin) are shown in the upper panel of Fig. 3. Within the RGM we do not start from a peculiar classical ground state. Moreover, the numerical computation of the spectrum has to be performed for each S value separately. As a result, we get S-dependent excitations $\omega_{\gamma\mathbf{q}}/S$, as we should expect using a more sophisticated approach. (Note that for the pyrochlore-lattice quantum Heisenberg ferromagnet the ground-state excitations energies $\omega_{\gamma\mathbf{q}}/S$ do not depend on S since the ground state is classical [52]). For finite S the differences to the linear-spin-wave spectrum of [71] are obvious: the flat (dispersionless) branch (green) is not the lowest one. It is twofold degenerate (as that of linear spin-wave theory for the collinear state) and its energy tends to zero as S increases (Fig. 3, lower panel) thus approaching the linear-spin-wave result. There are also two dispersive branches, one is gapless (red) and one is gapped (blue), which approach each other as S increases, i.e., again linear-spin-wave result is obtained for $S \to \infty$ (Fig. 3, lower panel). Apparently, the RGM decoupling procedure (that is not biased in favor of a classical ground state) is in favor of linear-spin-wave theory starting from the collinear classical state [71], but not necessarily a $\mathbf{q} = \mathbf{0}$ state (see our discussion in Sec. V).

For a similar discussion of the relation between excitation energies as they follow from the RGM and the linear-spin-wave theory for the kagome HAFM, see Ref. [66]. The ground-state excitation velocity v/S corresponding to the linear expansion of the lowest branch $\omega_{4\mathbf{q}}$ around the Γ point is shown in the inset of the lower panel of Fig. 3. Similar as for the kagome HAFM [66], v/S decreases with growing S. Note that in the next section we consider the temperature dependence of the excitation energies for the PHAF (see Fig. 13).

Let us turn to the spin-spin correlation functions. In Fig. 4 we show all nonequivalent ground-state correlators $\langle\hat{\mathbf{S}}_\mathbf{0}\cdot\hat{\mathbf{S}}_\mathbf{R}\rangle/[S(S+1)]$ up to a separation $R = |\mathbf{R}| = 3d$ for $S = \frac{1}{2}, 1, \frac{3}{2}, 3$. [We use here the scaling factor $S(S+1)$ because it leads to an S-independent ground-state correlator for the isolated spin dimer with antiferromagnetic coupling]. Since for a certain separation R inequivalent sites exist, more than one data point can appear at one and the same separation R

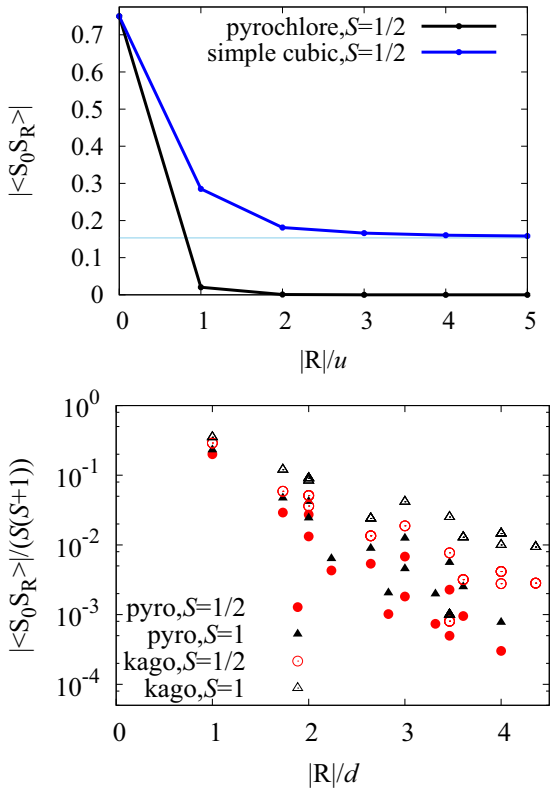

FIG. 5. (Top) The absolute value of the ground-state correlation functions $|\langle \hat{\mathbf{S}}_\mathbf{0} \cdot \hat{\mathbf{S}}_\mathbf{R} \rangle|$ as a function of the scaled distance $|\mathbf{R}|/u$ along the direction $(0, \frac{1}{2}, \frac{1}{2})$ for the $S = \frac{1}{2}$ PHAF ($u = 1/\sqrt{2}$, black) and for the $S = \frac{1}{2}$ simple-cubic HAFM along the direction (1,0,0) ($u = 1$, blue). (Bottom) The absolute value of the ground-state correlation functions $|\langle \hat{\mathbf{S}}_\mathbf{0} \cdot \hat{\mathbf{S}}_\mathbf{R} \rangle|/[S(S+1)]$ as a function of the separation $|\mathbf{R}|$ (scaled by the nearest-neighbor separation d) for the pyrochlore lattice ($d = \sqrt{2}/4 \approx 0.35$, filled symbols) and for the kagome lattice [66] ($d = 1$, open symbols) for $S = \frac{1}{2}$ (red) and $S = 1$ (black).

(e.g., for the third-neighbor separation $R = \sqrt{2}/2$ there are two kinds of correlators, which have different signs). Note that the signs of the correlators coincide with the results of Ref. [9] (see Table I in that paper). The fast decay of the correlation functions is obvious and it is also demonstrated in Fig. 5, where we compare the PHAF with the corresponding unfrustrated HAFM on the simple-cubic lattice (top) as well as with the two-dimensional kagome HAFM [66] for spin-quantum numbers $S = \frac{1}{2}$ and 1 (bottom; note the logarithmic scale of the y axis). The comparison with the simple-cubic lattice demonstrates the existence of a finite condensation term $C_{\mathbf{Q}=(\pi,\pi,\pi)}$ for this lattice as well as the lack of long-range order for the PHAF. These data may suggest an exponential decay. Interestingly, our data also suggest that the decay of the correlation functions is faster for the PHAF. To estimate the correlation length for the PHAF, we assume such an exponential decay. Then, a correlation length ξ can be extracted using the ansatz $|\langle \hat{\mathbf{S}}_\mathbf{0} \cdot \hat{\mathbf{S}}_\mathbf{R} \rangle| \propto \exp(-|\mathbf{R}|/\xi)$ (see Ref. [8]). Further, we fix the direction of $\mathbf{R}$ to $\mathbf{u} = (0, \frac{1}{2}, \frac{1}{2})$, i.e., $\mathbf{R} = n\mathbf{u}$, to have only one correlator for each separation $R = |\mathbf{R}|$, and consider the correlators until $n = 12$. Using the fitting function $f(R) = a\exp(-R/b) + c$ we get $b = 0.1963(\pm 0.09\%)$, i.e., $\xi(T = 0, S = \frac{1}{2}) \approx 0.20$. The increase of the quantum-spin number S leads to a slight increase of $|\langle \hat{\mathbf{S}}_\mathbf{0} \cdot \hat{\mathbf{S}}_\mathbf{R} \rangle|/[S(S+1)]$ (cf. Figs. 4 and 5, bottom). For $S = 1$ we find $b = 0.2233(\pm 0.10\%)$, i.e., $\xi(T = 0, S = 1) \approx 0.22$, and for $S = 3$ we find $b = 0.2578(\pm 0.38\%)$, i.e., $\xi(T = 0, S = 3) \approx 0.26$. (Note that the fitting constant c is always smaller than 10^{-4}). Thus, the correlation length is less than the nearest-neighbor separation and it is even smaller than for the kagome HAFM [66] (see also Fig. 5, bottom). In Fig. 6 we report the temperature dependence for the correlation length ξ for $S = \frac{1}{2}$ and 1. $\xi(T)$ shows a small maximum at low temperatures and then decreases with further temperature increase, as expected. We mention that a similar low-temperature maximum in $\xi(T)$ was also found for $S = \frac{1}{2}$ in Ref. [8].

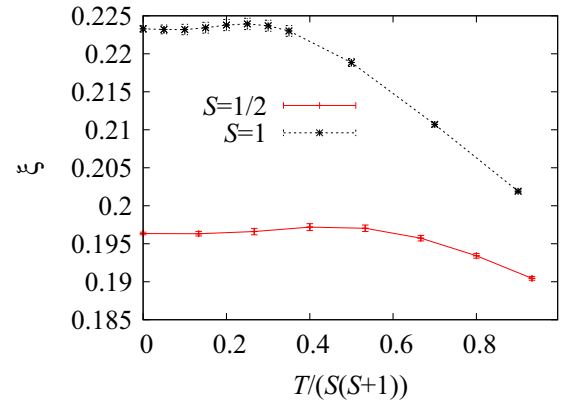

FIG. 6. Correlation length ξ as a function of the normalized temperature $T/[S(S+1)]$ ($J = 1$) for $S = \frac{1}{2}$ (red) and $S = 1$ (black).

An intensity plot of the static structure factor $S_\mathbf{q}$ [see, e.g., Eq. (3.11)] is shown in Fig. 7 within two planes in the $\mathbf{q}$ space, namely, the $(q_x = q_y) - q_z$ plane (left column) and in the plane $q_x - q_y$ for $q_z = 0$ (right column). $S_\mathbf{q}$ exhibits some typical features related to spin-liquid ground states, which are partially also present for the kagome HAFM. It is worth mentioning that similar features can be seen in experiments on $S = 1$ PHAF compound $NaCaNi_2F_7$ [see Fig. 1 and the left quadrants of Fig. 4(c) of Ref. [75]]. To compare with measured data, we notice that the neutron momentum transfer denoted in Ref. [75] as (h, k, l) corresponds to $(q_x/(2\pi), q_y/(2\pi), q_z/(2\pi))$ and thus, e.g., the vector (0,0,2) of Ref. [75] is the vector $(0, 0, 4\pi)$ in our notations. The pinch points at, e.g., $\mathbf{Q}_0 = (4\pi, 4\pi, 0)$ and other symmetry related points such as $(0, 0, 4\pi)$, indicate that in the classical limit each tetrahedron has vanishing total magnetization (ice rule). Along a continuous line (within the $q_z = 0 - q_x - q_y$ plane) indicated by the black squares (see the right panels of Fig. 7), the structure factor $S_\mathbf{q}/[S(S+1)]$ is maximal, which also means that (within the numerical precision of our RGM data) $S_\mathbf{q}/[S(S+1)]$ is constant on this line. This remains true for the RGM data at $T > 0$ (see Fig. 17). Obviously, the pinch points are located on this line of maximal $S_\mathbf{q}$.

For a quantitative analysis of the pinch points, we show in Fig. 8 the structure factor along a horizontal and a vertical momentum cut through the pinch point at $(0, 0, 4\pi)$. Since the pinch points are still present at finite temperatures, we show in Fig. 8, in addition to $T = 0$, also RGM and HTE

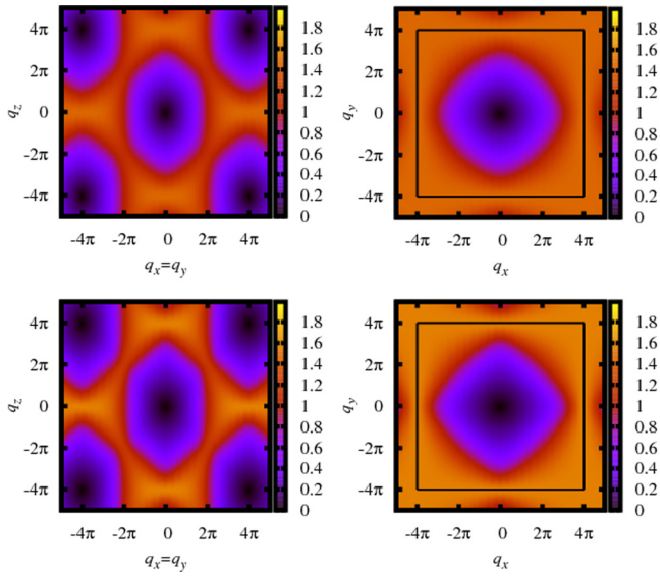

FIG. 7. Normalized static structure factor $S_{\mathbf{q}}/[S(S+1)]$ of the PHAF obtained within the RGM at $T=0$ for $S=\frac{1}{2}$ (top) and $S=1$ (bottom). We consider the two planes $q_y=q_x$ (left) and $q_z=0$ (right) within the (extended) Brillouin zone. The black squares in the right panels show the $\mathbf{q}$ points which yield the (same) maximal value of $S_{(q_x,q_y,0)}$.

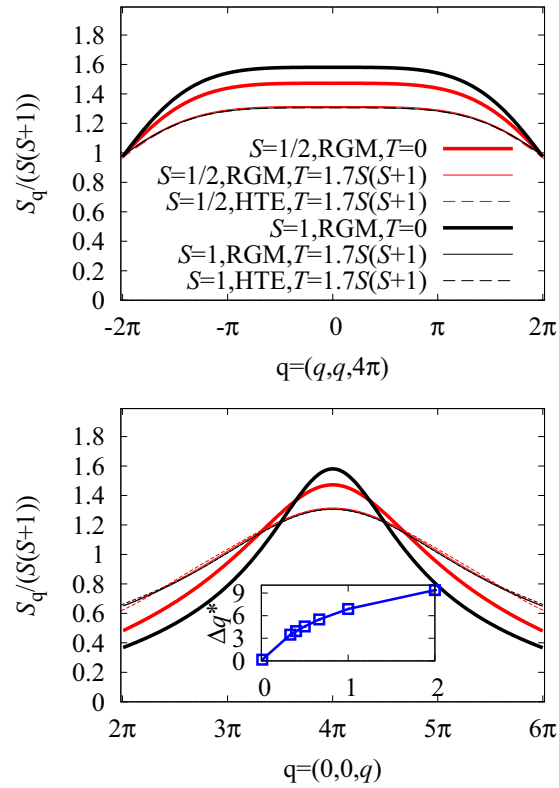

FIG. 8. Horizontal cut $(q,q,4\pi)$ (top) and vertical cut $(0,0,q)$ (bottom) through the pinch point at $(0,0,4\pi)$ for $S=\frac{1}{2}$ (red) and $S=1$ (black). RGM results at $T=0$ are shown by thick lines. We also show the results at $T=1.7S(S+1)$ by thin lines (solid lines correspond to RGM results and dashed lines correspond to HTE results) (see also Sec. V). Note that all thin lines for $T=1.7S(S+1)$ almost coincide. The inset (bottom) shows RGM results for the width-at-half-maximum of the pinch point Δq^* as a function of $1/S$ at $T=0$.

data at $T=1.7S(S+1)$. At $T=0$ the difference between $S=\frac{1}{2}$ and 1 is noticeable, but there is practically no difference between the two cases at $T=1.7S(S+1)$. Moreover, the agreement between RGM and HTE data at this temperature is very good. Along the horizontal cut, $S_{\mathbf{q}}/[S(S+1)]$ remains almost constant in a pretty wide region of q values. Along the vertical cut across the pinch point the sharpening of $S_{\mathbf{q}}/[S(S+1)]$ as S increases from $\frac{1}{2}$ to 1 is obvious [see the thick red and black lines in Fig. 8, bottom (see also Fig. 17 in Sec. V)]. To quantify this sharpening, we plot in the inset in Fig. 8 (bottom) the width of the pinch point at the half of the maximum Δq^* as a function of $1/S$ at $T=0$. Note that in the classical limit the pinch points become sharper as $\sqrt{T}$ as T decreases (see Ref. [25]). The sharpening of the pinch points is related to the decreasing role of quantum fluctuation as S increases. Only in the classical limit the ice rule is strictly valid (i.e., each tetrahedron can have vanishing total spin), whereas perfect spin-singlet formation on all tetrahedra is not possible in the quantum model since the total spin of a tetrahedron does not commute with the Hamiltonian. Note that similar features were observed in Ref. [24]. Although Iqbal *et al.* [24] discuss the $\mathbf{q}$-dependent susceptibility instead of the static structure factor, we may compare our data for the width-at-half-maximum Δq^* with those of Ref. [24] (see Figs. 7 and 8 in [24]). For $S=\frac{1}{2}$ the zero-temperature width-at-half-maximum (i.e., $\chi/\chi_{\max}=0.5$ in Ref. [24] and $S_{\mathbf{q}}/[S(S+1)]\approx 0.74$ in our paper) is around $\Delta q^*\approx 2.7\pi$ according to the RGM that is about 140% of the PFFRG data. For $S=1$ we have $\Delta q^*\approx 2.0\pi$ that is about 120% of the PFFRG data. In the limit $S\to\infty$ the RGM yields correct value $\Delta q^*=0$. At the finite temperature $T=1.7S(S+1)$ for $S=\frac{1}{2}$, 1 the RGM data and the HTE data for Δq^* are indistinguishable but apparently are slightly larger than the PFFRG ones.

Next, we consider the dynamical structure factor $S^{zz}_{\mathbf{q}}(\omega)$ [see Eq. (3.8)]. While dynamical quantities for the quantum HAFM on the kagome lattice were discussed in several theoretical papers (see, e.g., Refs. [76–78]), corresponding results for the quantum PHAF are scarce. Very recently, a combination of molecular dynamics simulations, stochastical dynamical theory, and linear-spin-wave theory has been used for a theoretical study of the dynamical structure factor of the spin-1 pyrochlore material $NaCaNi_2F_7$ [25]. Corresponding experimental data for the dynamical properties of $NaCaNi_2F_7$ can be found in Ref. [75]. Here, we also use the experimental data shown in Figs. 2 and 3 of Ref. [75] as a guideline for the presentation of our RGM results for $S^{zz}_{\mathbf{q}}(\omega)$ given in Figs. 9–12. To connect our calculations to this compound, we recall that for $NaCaNi_2F_7$ the estimate for J is about 3.2 meV (37 K). Then, the experiments at $T=1.5$ K correspond to $T/J\approx 0.04$ in our study and the energy transfers 2, 8, and 12 meV correspond to $\omega/J\approx 0.625$, 2.5, and 3.75, respectively. We also recall that the neutron momentum transfer denoted in Ref. [75] as (h,k,l) corresponds to $(q_x/(2\pi), q_y/(2\pi), q_z/(2\pi))$ in our notations.

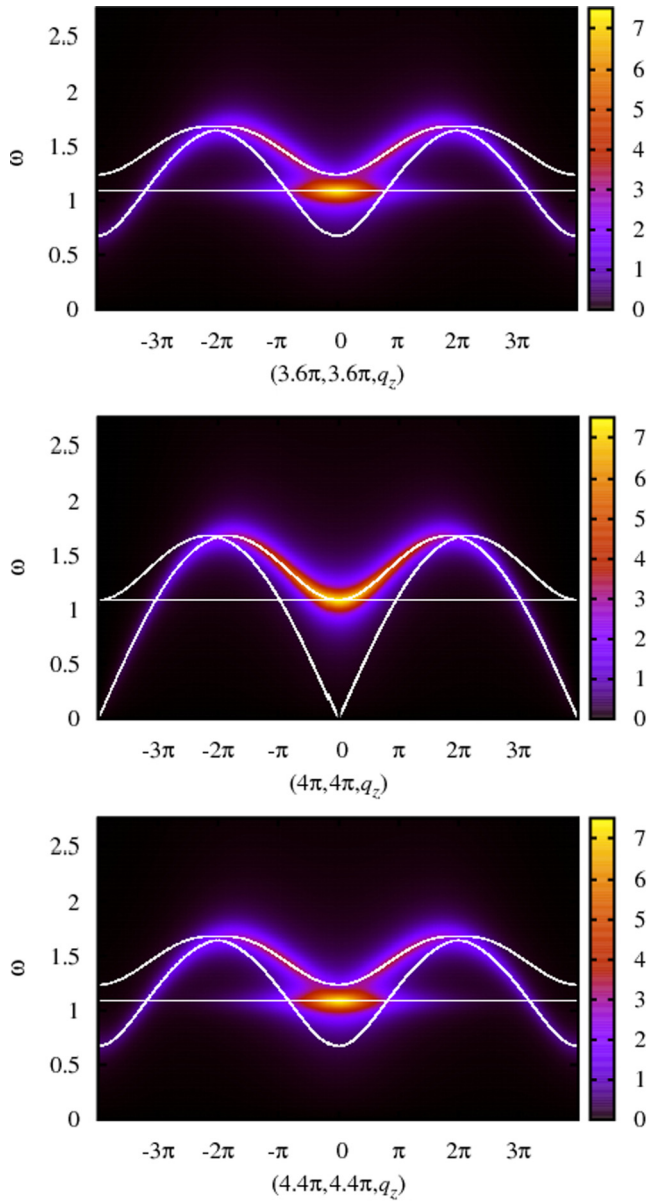

FIG. 9. Dynamical structure factor $S^{zz}_{\mathbf{q}}(\omega)$ of the $S = \frac{1}{2}$ PHAF ($J = 1$) at $q_x = q_y = 3.6\pi, 4\pi, 4.4\pi$ along the line $-4\pi \leqslant q_z \leqslant 4\pi$ for $T = 0$. We set $\epsilon = 0.1$. The white lines correspond to the excitation energies $\omega_{\gamma\mathbf{q}}$ (3.3).

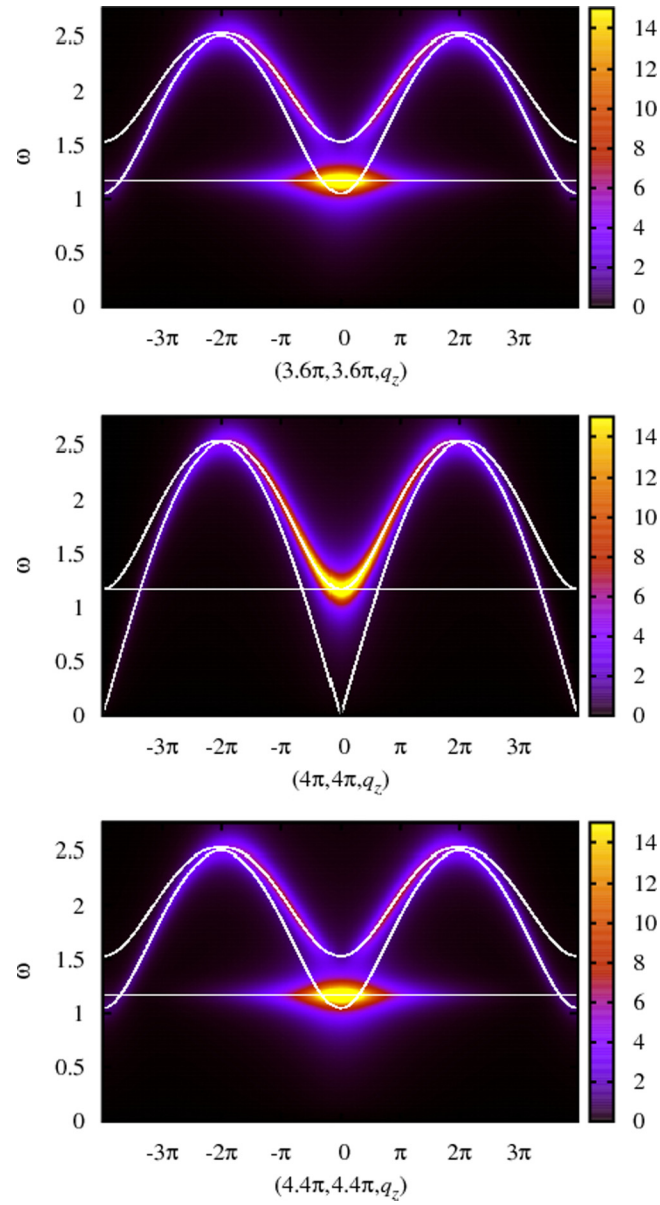

FIG. 10. Dynamical structure factor $S^{zz}_{\mathbf{q}}(\omega)$ of the $S = 1$ PHAF ($J = 1$) at $q_x = q_y = 3.6\pi, 4\pi, 4.4\pi$ along the line $-4\pi \leqslant q_z \leqslant 4\pi$ for $T = 0$. We set $\epsilon = 0.1$. The white lines correspond to the excitation energies $\omega_{\gamma\mathbf{q}}$ [Eq. (3.3)]. These theoretical plots may be compared to experimental data reported in the left part of Fig. 3(a) of Ref. [75].

We begin with the momentum cut along $(4\pi, 4\pi, q_z)$ [see Figs. 9 (for $S = \frac{1}{2}$) and 10 (for $S = 1$) and the corresponding Fig. 3(a) of Ref. [75]]. Except for the low-frequency region, our theoretical predictions look similar to the experimental observations, both having a kind of vertical fountain structure with the origin at $\mathbf{q} = (4\pi, 4\pi, q_z = 0)$ and $\omega \approx J$. The nonzero values of $S^{zz}_{\mathbf{q}}(\omega)$ at $\mathbf{q} = (4\pi, 4\pi, q_z)$ shown in the middle panels of Figs. 9 ($S = \frac{1}{2}$) and 10 ($S = 1$) are (nonuniformly) concentrated only along the dispersive branch $\omega_{3\mathbf{q}}$ with $|q_z| \leqslant 2\pi$. Since experiments give the scattering cross section at (q, q, q_z) with $3.6\pi < q < 4.4\pi$, we show in Figs. 9 and 10 theoretical predictions for $q = 3.6\pi$ (upper panels) and $q = 4.4\pi$ (lower panels), too. These slight deviations from $q_x = q_y = 4\pi$ change the scattering dramatically. Namely, the dynamical structure factor is now concentrated mostly along the dispersionless excitation branch $\omega_{1\mathbf{q}} = \omega_{2\mathbf{q}}$ around $|q_z| \leqslant \pi$. Although the dispersive branch $\omega_{3\mathbf{q}}$ is still visible, the value of $S^{zz}_{\mathbf{q}}(\omega)$ along this branch is relatively small. The comparison of the cases $S = \frac{1}{2}$ and 1 does not show qualitative differences, however, all features for the latter case are much sharper.

For another momentum cut, $\mathbf{q} = (q, q, 4\pi)$ [see Figs. 11 and 12 and the corresponding Fig. 3(a) of Ref. [75]], $S^{zz}_{\mathbf{q}}(\omega)$ is again concentrated along one excitation branch, but now along the dispersionless one $\omega_{1\mathbf{q}} = \omega_{2\mathbf{q}}$ with $|q| \leqslant 2\pi$. When q_z deviates from 4π (in experiments $3.6\pi < q_z < 4.4\pi$), $S^{zz}_{\mathbf{q}}(\omega)$

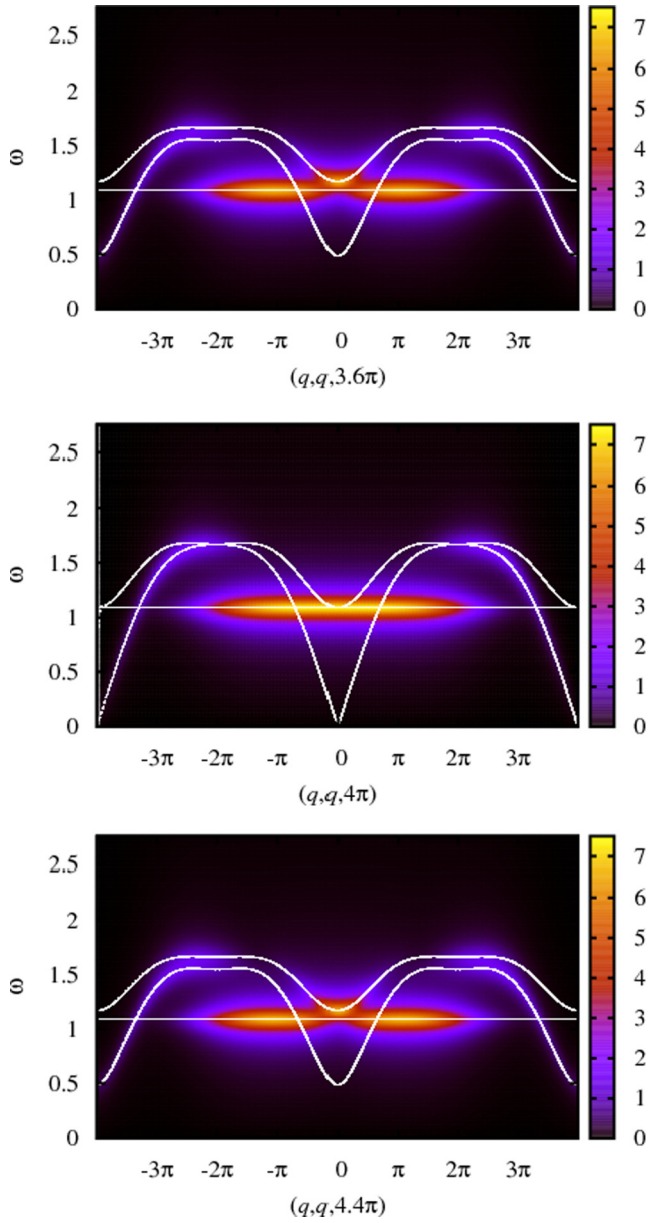

FIG. 11. Dynamical structure factor $S^{zz}_{\mathbf{q}}(\omega)$ of the $S = \frac{1}{2}$ PHAF ($J = 1$) at $q_z = 3.6\pi, 4\pi, 4.4\pi$ along the line $-4\pi \leqslant q_x = q_y \leqslant 4\pi$ for $T = 0$. We set $\epsilon = 0.1$. The white lines correspond to the excitation energies $\omega_{\gamma\mathbf{q}}$ [Eq. (3.3)].

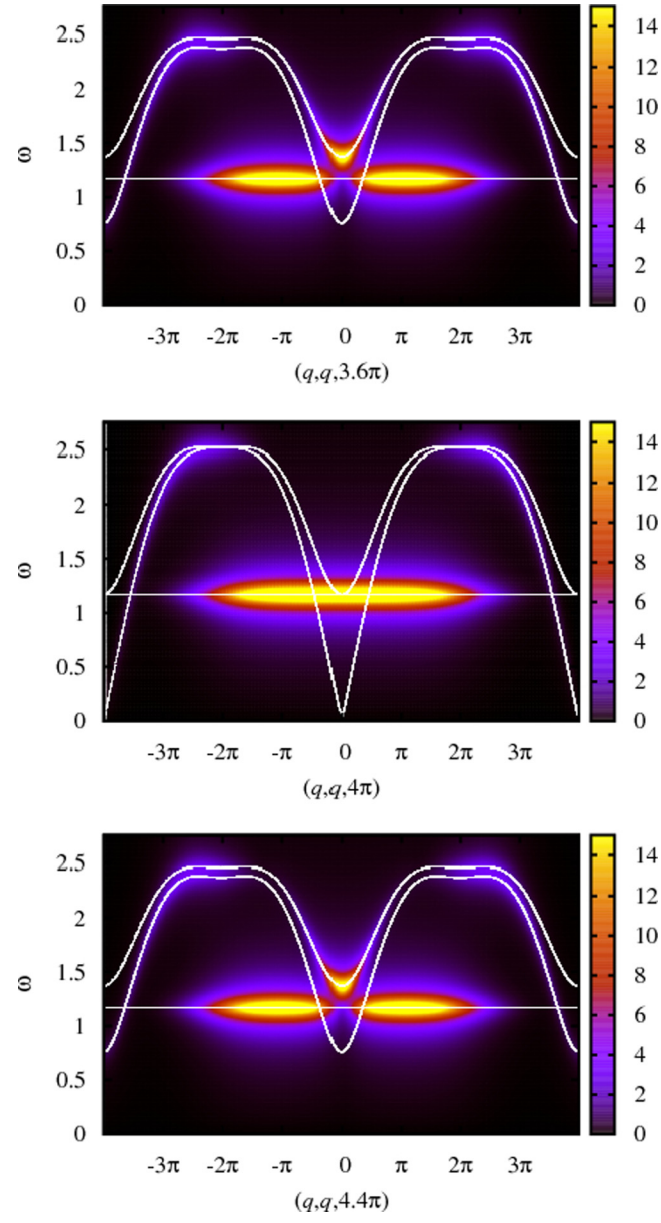

FIG. 12. Dynamical structure factor $S^{zz}_{\mathbf{q}}(\omega)$ of the $S = 1$ PHAF ($J = 1$) at $q_z = 3.6\pi, 4\pi, 4.4\pi$ along the line $-4\pi \leqslant q_x = q_y \leqslant 4\pi$ for $T = 0$. We set $\epsilon = 0.1$. The white lines correspond to the excitation energies $\omega_{\gamma\mathbf{q}}$ [Eq. (3.3)]. Our theoretical plots may be compared to experimental data reported in the right part of Fig. 3(a) of Ref. [75].

redistributes in the q-ω plane, i.e., it vanishes along the dispersionless branch around $q = 0$, but emerges for these q values along the dispersive branch $\omega_{3\mathbf{q}}$. This looks similar to what can be seen in the experimental data around $\mathbf{q} = (q, q, 4\pi)$, $|q| \leqslant 2\pi$, and $\omega \approx J$ [cf. the right part of Fig. 3(a) of Ref. [75]]. Again, all features become sharper as S increases from $\frac{1}{2}$ to 1.

To conclude this discussion, apparently, the RGM results are similar to the experimentally observed features at 3 ...8 meV shown in the left and right parts of Fig. 3(a) of Ref. [75] (see Figs. 10 and 12, respectively). On the other hand, the $\mathbf{q}$-independent features below 2 meV present in the experiment are not found in our theory. We mention that a similar disagreement at low frequencies between theory and experiment was reported in Ref. [25]. A possible origin of this discrepancy may consist in disorder (there is Na^{1+}/Ca^{2+} charge disorder which is expected to generate a random variation in the magnetic exchange interactions) and/or further small terms in the Hamiltonian (the nearest-neighbor 3×3 exchange interaction matrix has three more components the values of which are, however, smaller than 0.1 meV) relevant for the specific magnetic compound studied in the experiment (see the corresponding discussion in Ref. [25]). These extra features may also contribute to the differences at 3 ...8 meV between measurement and theoretical results obtained for the pure model with only isotropic nearest-neighbor exchange.

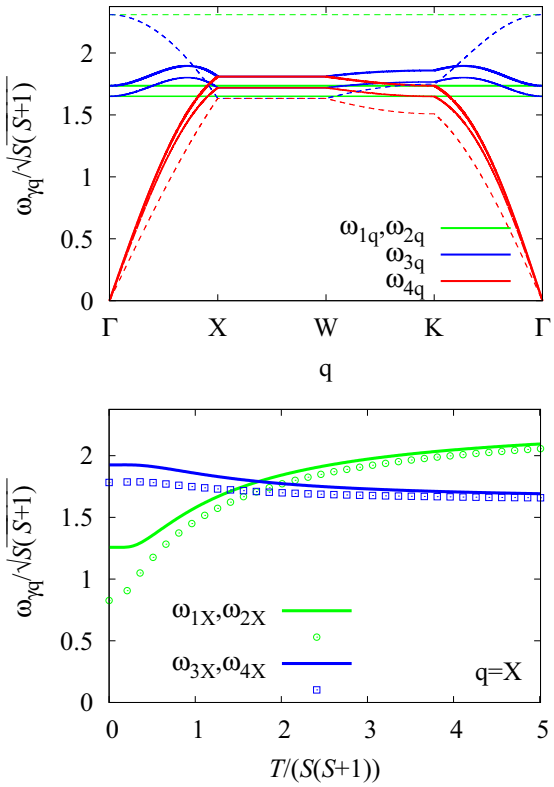

FIG. 13. (Top) Dispersion of the excitation energies $\omega_{\gamma\mathbf{q}}/\sqrt{S(S+1)}$ [Eq. (3.3), $J=1$] at temperature $T=1.5$ for $S=\frac{1}{2}$ (thick) and $S=1$ (thin) and in the infinite-temperature limit $T\to\infty$ (very thin dashed). Note that $\omega_{\gamma\mathbf{q}}/\sqrt{S(S+1)}$ is independent of S at $T\to\infty$. The points Γ, X, W, and K in the first Brillouin zone of a face-centered-cubic Bravais lattice are given by $\Gamma=(0,0,0)$, $\mathrm{X}=(0,2\pi,0)$, $\mathrm{W}=(\pi,2\pi,0)$, and $\mathrm{K}=(3\pi/2,3\pi/2,0)$ (see Fig. 1, bottom). (Bottom) Temperature dependence of the excitation energies $\omega_{\gamma\mathbf{q}}/\sqrt{S(S+1)}$ at the X point for $S=\frac{1}{2}$ (lines) and $S=1$ (symbols). Note that at the X point $\omega_{3\mathbf{q}}=\omega_{4\mathbf{q}}$ is valid for all temperatures.

Let us finally mention that the experimental data for the dynamical structure factor are obtained at a finite temperature $T=1.8$ K [75]. Bearing in mind the exchange constant $J\approx 3.2$ meV (37 K) of $NaCaNi_2F_7$, we have $T/[S(S+1)]\approx 0.025J$, which practically corresponds to zero temperature (see Fig. 13), where the temperature dependence of the excitation spectrum is shown.

V. FINITE-TEMPERATURE PROPERTIES

In this section we consider only the extreme quantum cases $S=\frac{1}{2}$ and 1 and report below the RGM results along with the HTE results. As mentioned in Sec. IV and discussed in Ref. [66] the minimal version considered here works best for low spin-quantum numbers S. Moreover, for the particular cases of the kagome HAFM and the PHAF for larger S, the RGM equations may lead at finite temperatures to unphysical poles in the specific heat [79]. To overcome this drawback, one needs an additional input to open the possibility to consider more vertex parameters [66].

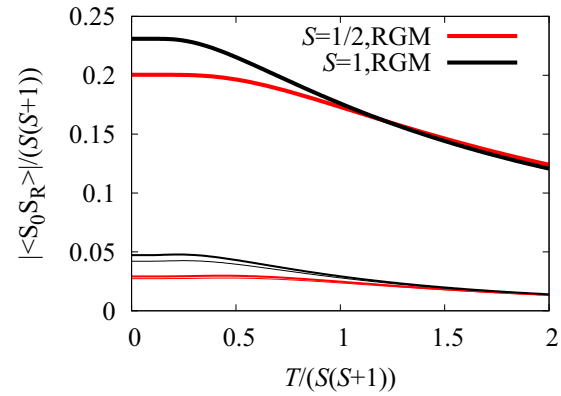

FIG. 14. The absolute value of correlation functions $|\langle\hat{\mathbf{S}}_\mathbf{0}\cdot\hat{\mathbf{S}}_\mathbf{R}\rangle|/[S(S+1)]$ between nearest neighbors (thick), next-nearest neighbors (normal), and between third-nearest neighbors straight along two bonds (thin) as a function of the normalized temperature $T/[S(S+1)]$ ($J=1$) for $S=\frac{1}{2}$ (red) and $S=1$ (black). Note that for $S=\frac{1}{2}$ the next-nearest- and third-nearest-neighbor correlators almost coincide.

We start with the discussion of the RGM results for the excitations. As mentioned above, the RGM provides an improved description of the excitation spectrum compared to linear-spin-wave theory. Since the excitation energies $\omega_{\gamma\mathbf{q}}$ contain spin correlation functions c_{ijk} [cf. Eq. (3.3)], they are temperature dependent. At $T\to\infty$, we have $c_{ijk}=0$ resulting in the simplified expressions $\omega_{1\mathbf{q}}^2/J^2=\omega_{2\mathbf{q}}^2/J^2=16S(S+1)/3$, $\omega_{3\mathbf{q}}^2/J^2=4S(S+1)(2+D_\mathbf{q})/3$, and $\omega_{4\mathbf{q}}^2/J^2=4S(S+1)(2-D_\mathbf{q})/3$. Note that in this limit $\omega_{\gamma\mathbf{q}}^2$ does not depend on the sign of J and scales as $S(S+1)$. The branches of the spectrum (3.3) in the ground state shown in Fig. 3, top, can be compared with those shown in Fig. 13, top, for $T\to\infty$ and for $T=1.5$. The temperature dependence of the dispersive bands at the X point and of the flat bands are shown in Fig. 13, bottom. Note that the flat-band excitations increase monotonously with T and become the highest-energy ones at about $T/[S(S+1)]\approx 1.8$.

RGM data for the temperature dependence of the spin correlations for nearest, next-nearest, and third neighbors are presented in Fig. 14. These short-range correlators show almost no dependence on T at low temperatures. For the nearest-neighbor and next-nearest-neighbor correlators the decrease of $|\langle\hat{\mathbf{S}}_\mathbf{0}\cdot\hat{\mathbf{S}}_\mathbf{R}\rangle|/[S(S+1)]$ for $T/[S(S+1)]\gtrsim 0.5$ is noticeable. For the third-neighbor correlator (being already very small at $T=0$), the influence of T is very weak.

Next, we present in Fig. 15 the RGM and the HTE results for the temperature dependence of the specific heat $C_V(T)$. Clearly, there is a relation between the temperature profile of the nearest-neighbor correlator (internal energy) (Fig. 14) and that of the specific heat (Fig. 15). In the high-temperature region the HTE and the RGM results coincide down to about $T/[S(S+1)]\approx 1$. The temperature profile $C_V(T)$ is typical for spin systems with only short-range order. The increase and the shift of the main maximum with growing S known for the kagome HAFM [66] is also present for the PHAF (cf. also Ref. [68]). At low temperatures for strongly frustrated quantum magnets unconventional features in the temperature

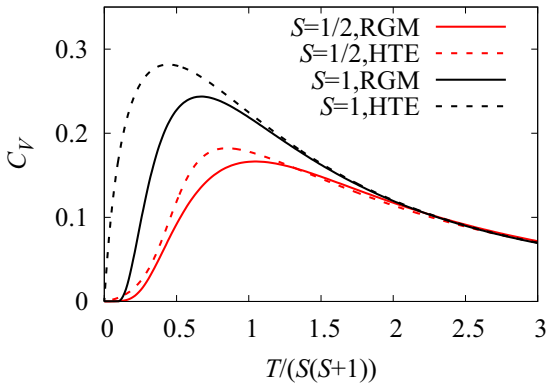

FIG. 15. Specific heat of the PHAF obtained by RGM (solid) and HTE (dashed, Padé [6,7] for $S = \frac{1}{2}$ and Padé [5,6] for $S = 1$) as a function of the normalized temperature $T/[S(S+1)]$ ($J = 1$) for $S = \frac{1}{2}$ (red) and $S = 1$ (black).

profile of the specific heat, such as shoulders or additional maxima, may appear (see, e.g., Refs. [80–84]). We do not find such peculiar features for the PHAF within our RGM approach. However, we do not claim that the RGM is able to detect the subtle role of low-lying excitations relevant for such particular low-temperature properties.

A straightforward outcome from the RGM equations is the susceptibility $\chi_{\mathbf{Q}}$ given in Eq. (3.7). In Fig. 16 we report the temperature dependence of the uniform susceptibility $\chi_{\mathbf{0}}$ of the $S = \frac{1}{2}$ and 1 PHAF obtained within the RGM and HTE approaches. Again at high temperatures the results of both approaches coincide. The temperature dependence of $\chi_{\mathbf{0}}$ is smooth and the typical maximum is weakly pronounced.

A quantity of high interest in frustrated magnets is the (static) magnetic structure factor (3.11) which is related to an experimentally accessible quantity, the differential magnetic neutron cross section $d\sigma/d\Omega$. Already in Fig. 7 we have presented a contour plot of the ground-state structure factor of the PHAF in two planes of the $\mathbf{q}$ space, namely, $q_x = q_y$ (left panels) and $q_z = 0$ (right panels). Since the spin correlations are already at zero temperature extremely short ranged, the

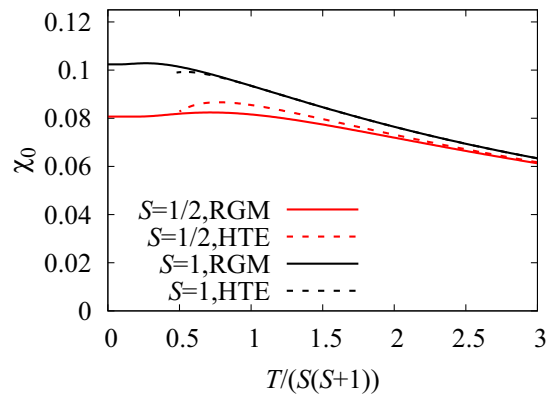

FIG. 16. Uniform susceptibility of the PHAF within the RGM (solid) and the HTE (dashed, Padé [6,7] for $S = \frac{1}{2}$ and Padé [5,6] for $S = 1$) as a function of the normalized temperature $T/[S(S+1)]$ ($J = 1$) for $S = \frac{1}{2}$ (red) and $S = 1$ (black).

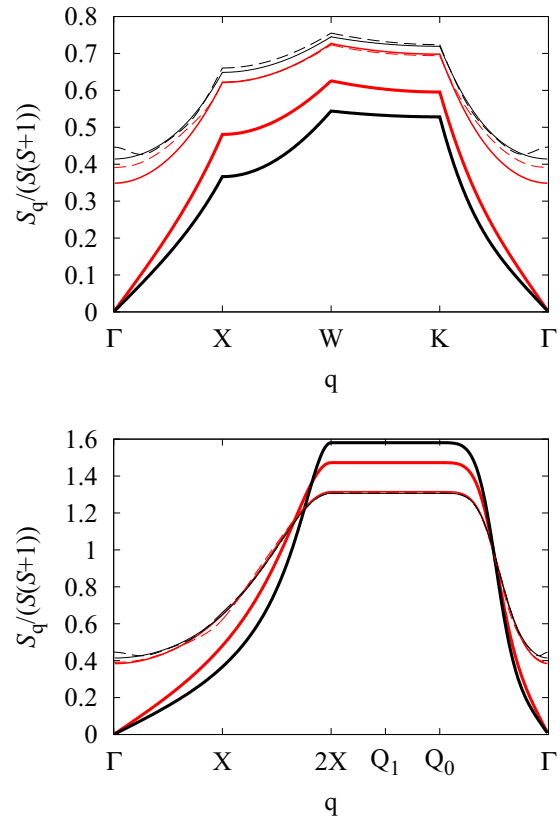

FIG. 17. Normalized static structure factor $S_{\mathbf{q}}/[S(S+1)]$ along two paths in $\mathbf{q}$ space for $S = \frac{1}{2}$ (red) and $S = 1$ (black) obtained within RGM (solid) at $T = 0$ (thick) and $T = 1.7S(S+1)$ (thin) compared with HTE data for $T = 1.7S(S+1)$ (thin dashed, 12th order for $S = \frac{1}{2}$ and 10th order for $S = 1$). Here, $\Gamma = (0, 0, 0)$, $\mathrm{X} = (0, 2\pi, 0)$, $\mathrm{W} = (\pi, 2\pi, 0)$, and $\mathrm{K} = (3\pi/2, 3\pi/2, 0)$ (see Fig. 1, bottom). The points $2\mathrm{X} = (0, 4\pi, 0)$, $\mathbf{Q}_1 = (2\pi, 4\pi, 0)$, and $\mathbf{Q}_0 = (4\pi, 4\pi, 0)$ are located along the upper line of the black square in the right part of Fig. 7.

influence of T on $S_{\mathbf{q}}$ is weak and the basic features of $S_{\mathbf{q}}$ shown in Fig. 7 survive at moderate temperatures. To get a more quantitative information on the temperature dependence of $S_{\mathbf{q}}$ we compare the $\mathbf{q}$ dependence of the structure factor for $T = 0$ and $1.7S(S+1)$ for $S = \frac{1}{2}$ and 1 in Fig. 17. Here, the $\mathbf{q}$ line chosen for the upper panel is the same as in Figs. 3 and 13, whereas the $\mathbf{q}$ line chosen for the lower panel contains the path along which the structure factor reaches its maximal value $S_{\mathbf{q}}^{\max}$ (see the black-square line in the right panels of Fig. 7). As can be seen from Fig. 17, the line of maximal $S_{\mathbf{q}}$ remains horizontal at finite T and $S_{\mathbf{q}}^{\max}$ decreases only by 11% (17%) for $S = \frac{1}{2}$ ($S = 1$) as increasing the temperature from $T = 0$ to $1.7S(S+1)$. We mention that the temperature dependence of momentum cuts through a pinch point can be found in Fig. 8.

It is obvious from Fig. 17 that the static structure factors of the PHAF obtained by the RGM and the HTE are in good agreement for the selected temperature of $T = 1.7S(S+1)$, where the 12th-order HTE for $S = \frac{1}{2}$ is reliable in the whole Brillouin zone. For $S = 1$ we only can present data for the 10th-order HTE. Although the overall agreement in this case

TABLE I. First nine HTE terms of the static structure factor $s_{\mathbf{q},S,n}/\{[S(S+1)]^{n+1}J^n\}$ for $\mathbf{q}=(q_x,4\pi,0)$ for the spin-S PHAF with $S=\frac{1}{2}$, 1, and $\frac{3}{2}$.

n	$S=\frac{1}{2}$	$S=1$	$S=\frac{3}{2}$
1	$\frac{2}{3}$	$\frac{2}{3}$	$\frac{2}{3}$
2	0	$-\frac{5}{36}$	$-\frac{8}{45}$
3	$-\frac{20}{27}$	$-\frac{10}{27}$	$-\frac{2588}{10125}$
4	$\frac{62}{243}$	$\frac{1721}{5184}$	$\frac{8662}{30375}$
5	$\frac{1312}{1215}$	$\frac{133}{810}$	$\frac{84448}{3796875}$
6	$-\frac{28006}{32805}$	$-\frac{32309}{69120}$	$-\frac{142434998}{512578125}$
7	$\frac{-1031308-560\cos\frac{q_x}{2}}{688905}$	$\frac{6039471-4480\cos\frac{q_x}{2}}{39191040}$	$\frac{11132918004-1750000\cos\frac{q_x}{2}}{53820703125}$
8	$\frac{4423862+3608\cos\frac{q_x}{2}}{2066715}$	$\frac{1552120827+633088\cos\frac{q_x}{2}}{3762339840}$	$\frac{552725758-498920\cos\frac{q_x}{2}}{6458484375}$
9	$\frac{18947028+8576\cos\frac{q_x}{2}}{11160261}$	$\frac{-573191935+107488\cos\frac{q_x}{2}}{1128701952}$	$\frac{-31183199780044+38350832000\cos\frac{q_x}{2}}{108986923828125}$

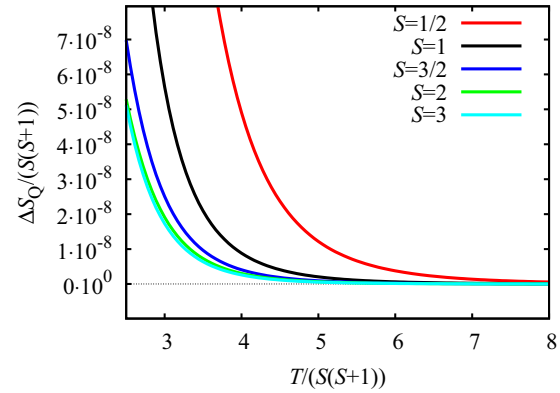

FIG. 18. Difference of the static structure factor $\Delta S_{\mathbf{Q}}=S_{\mathbf{Q}_1}-S_{\mathbf{Q}_0}$ [scaled by $S(S+1)$] with $\mathbf{Q}_1=(2\pi,4\pi,0)$ and $\mathbf{Q}_0=(4\pi,4\pi,0)$ within the HTE approach for $S=\frac{1}{2}$ (12th order) and $S=1,\frac{3}{2},2,3$ (10th order) as a function of the normalized temperature $T/[S(S+1)]$.

is still good, the HTE shows slight oscillations near the Γ point $\mathbf{q}\approx\mathbf{0}$. We also mention that our $S_{\mathbf{q}}$ data are in good agreement with recent PFFRG results (see Fig. 14 in Ref. [24]).

As mentioned in Sec. IV, within the numerical accuracy of the RGM the magnitude of the static structure factor along the black square in the right panels of Fig. 7 (line of maximal height, including the points 2X, $\mathbf{Q}_1$, and $\mathbf{Q}_0$) is the same (cf. also the lower panel in Fig. 17). Although the HTE treatment is restricted to high temperatures, nevertheless, it may provide rigorously some important information about the PHAF properties, such as *order by disorder* selection of magnetic structures. We will use the analytical HTE expressions for $S_{\mathbf{q}}$ to extract information on the behavior of the structure factor along the line of maximal height. We also go beyond the extreme quantum cases $S=\frac{1}{2}$, 1 and show results for $S>1$ for comparison. In Table I we present the HTE series of $S_{\mathbf{q}}$ up to the ninth order along the line $\mathbf{q}=(q_x,4\pi,0)$ including the points 2X, $\mathbf{Q}_1$, and $\mathbf{Q}_0$. (In the Appendix, we provide the first three HTE terms of the PHAF static structure factor at arbitrary $\mathbf{q}$ points). We observe that the $\mathbf{q}$ dependence [term $\cos(q_x/2)$] starts with order 7. The extreme values of the cosine are at $\mathbf{Q}_1$ and $\mathbf{Q}_0$. To quantify the variation of $S_{\mathbf{q}}$ we plot in Fig. 18 the difference $\Delta S_{\mathbf{Q}}=S_{\mathbf{Q}_1}-S_{\mathbf{Q}_0}$ as a function of temperature. We find indeed an *order by disorder* selection of the $\mathbf{Q}_1$ structure, although the magnitude of $\Delta S_{\mathbf{Q}}$ is small. This result is in agreement with the findings of Canals and Lacroix [8,9] and the corresponding spin structure is a collinear phase [see the inset of Fig. 3 in Ref. [8]], where (classically) the total spin vanishes on each tetrahedron and neighboring tetrahedra are dephased by π. We also find that $\Delta S_{\mathbf{Q}}$ is largest for the extreme quantum case. For larger spin quantum numbers $S=2$ and 3 the curves $\Delta S_{\mathbf{Q}}/[S(S+1)]$ versus $T/[S(S+1)]$ almost coincide. Let us mention here that the *order by disorder* selection due to thermal fluctuations discussed above is in accordance with the selection of collinear spin structures by quantum fluctuations found by large-S approaches [19–21] (see also our discussion of the excitation spectrum in Sec. IV).

VI. SUMMARY

We have presented a comprehensive study of the ground-state and finite-temperature static and dynamical properties of the spin-S PHAF using a rotation-invariant Green's function method (RGM) and the high-temperature expansion (HTE). The focus of our study is on the extreme quantum cases $S=\frac{1}{2}$ and 1.

The highly frustrated quantum PHAF is one of the most challenging problems in quantum magnetism. The toolbox to deal with this three-dimensional system is sparse. Thus, most of the methods appropriate for one- and two-dimensional systems (e.g., DMRG, exact diagonalization, finite-temperature Lanczos, tensor network) are not suitable in three dimensions. We believe that the application of existing universal many-body methods to the PHAF, such as Green's function technique, high-temperature expansion (both used in our paper), and the pseudofermion functional renormalization group method (used in Ref. [24]) is timely. All these methods have their specific limitations and it is highly desirable to compare the outcomes of these approaches to achieve progress in this field. At moderate and higher temperatures the comparison with the HTE data demonstrates that for those temperatures the RGM yields correct data. We admit that the accuracy of the method at low temperatures is not comparable with large-scale quantum Monte Carlo or DMRG. However, these precise many-body tools unfortunately are not applicable to the problem at hand.

To summarize some of our findings, we mention first that within our approaches we do not find indications of magnetic long-range order for all temperatures $T\geqslant 0$, including the absence of ground-state magnetic long-range order for arbitrary S. Already at $T=0$ the spin-spin correlations are extremely short ranged, leading to a correlation length that is below the nearest-neighbor separation. It is appropriate to mention that by means of the PFFRG approach [24], the analysis of the RG flow yields some indications for a finite-temperature transition for some intermediate values of $1<S<\infty$. However, the authors of that study were finally unable to conclude about the presence (or absence) of magnetic long-range order and/or

to determine the nature of the magnetic order (if any). In particular, in agreement with our study no divergence of the static structure factor $S_{\mathbf{q}}$ at any $\mathbf{q}$ vector was found. Second, the RGM approach gives a temperature-dependent excitation spectrum. We find two degenerate flat modes and two dispersive modes. By contrast to the linear-spin-wave theory [71], the flat modes are not the lowest ones, but approach zero energy as $S \to \infty$. Comparing our RGM energy dispersions at $T = 0$ with linear-spin-wave data of Ref. [71] one may conclude that the RGM data are in favor of collinear spin states. Third, the static structure factor has "spin-ice" features seen as pinch points [24,28] even at $T = 0$. Momentum cuts through the pinch points demonstrate that these points become sharper as S increases. Fourth, the RGM data of the dynamical structure factor are applicable to interpret neutron scattering data for the $S = 1$ pyrochlore compound $NaCaNi_2F_7$, however, with the exception of the lowest frequencies. Fifth, the HTE data for the $\mathbf{q}$ dependence of the static structure factor illustrate a weak *order by disorder* selection of a collinear spin structure that emerges as the temperature goes down from the infinite-temperature limit. The HTE analysis is rigorous within an appropriate (high-) temperature range $T/[S(S+1)] \lesssim J$ and may be used further to detect favored magnetic structures due to small extra interactions. Finally, the reported temperature dependencies of the spin correlations, the specific heat, and the uniform susceptibility obtained by RGM and HTE may provide useful benchmarks for further study of these properties by other methods.

ACKNOWLEDGMENTS

We acknowledge useful discussions with Y. Iqbal, P. McClarty, and R. Moessner. J.R. and O.D. thank the Wilhelm und Else Heraeus Stiftung for the kind hospitality at the 673. WE-Heraeus-Seminar "Trends in Quantum Magnetism" (Bad Honnef, 4-8 June 2018). O.D. acknowledges the kind hospitality of the MPIPKS, Dresden, and at the Workshop "Correlated Electrons in Transition-Metal Compounds: New Challenges." The work of O.D. was partially supported by Project FF-30F (Project No. 0116U001539) from the Ministry of Education and Science of Ukraine.

APPENDIX: FIRST TERMS OF THE STATIC STRUCTURE FACTOR WITHIN THE HTE

In this Appendix we provide explicit formulas for the first three terms of the HTE for the static structure factor. For $S = \frac{1}{2}$ we have

$$\begin{aligned}\frac{S_{\mathbf{q},S=1/2}}{S(S+1)} = 1 &- \frac{2J}{3\tilde{T}}\left(\cos\frac{q_x}{4}\cos\frac{q_y}{4} + \cos\frac{q_y}{4}\cos\frac{q_z}{4} + \cos\frac{q_x}{4}\cos\frac{q_z}{4}\right)\\ &+ \frac{2J^2}{9\tilde{T}^2}\left(\cos\frac{q_z}{2}\cos\frac{q_x}{2} + \cos\frac{q_y}{2}\cos\frac{q_z}{2} + \cos\frac{q_x}{2}\cos\frac{q_y}{2}\right)\\ &+ \frac{2J^2}{9\tilde{T}^2}\cos\frac{q_x}{4}\left(2\cos\frac{q_y}{2}+1\right)\cos\frac{q_z}{4} + \frac{2J^2}{9\tilde{T}^2}\cos\frac{q_x}{4}\cos\frac{q_y}{4}\left(2\cos\frac{q_z}{2}+1\right)\\ &+ \frac{2J^2}{9\tilde{T}^2}\left(2\cos\frac{q_x}{2}+1\right)\cos\frac{q_y}{4}\cos\frac{q_z}{4} + \cdots + \frac{s_{\mathbf{q},S=1/2,12}}{[S(S+1)]^{13}\tilde{T}^{12}}.\end{aligned} \tag{A1}$$

For $S = 1$ we have

$$\begin{aligned}\frac{S_{\mathbf{q},S=1}}{S(S+1)} = 1 &- \frac{2J}{3\tilde{T}}\left(\cos\frac{q_x}{4}\cos\frac{q_y}{4} + \cos\frac{q_y}{4}\cos\frac{q_z}{4} + \cos\frac{q_x}{4}\cos\frac{q_z}{4}\right)\\ &+ \frac{2J^2}{9\tilde{T}^2}\left(\cos\frac{q_z}{2}\cos\frac{q_x}{2} + \cos\frac{q_y}{2}\cos\frac{q_z}{2} + \cos\frac{q_x}{2}\cos\frac{q_y}{2}\right)\\ &+ \frac{2J^2}{9\tilde{T}^2}\cos\frac{q_x}{4}\left(2\cos\frac{q_y}{2}+\frac{13}{8}\right)\cos\frac{q_z}{4} + \frac{2J^2}{9\tilde{T}^2}\cos\frac{q_x}{4}\cos\frac{q_y}{4}\left(2\cos\frac{q_z}{2}+\frac{13}{8}\right)\\ &+ \frac{2J^2}{9\tilde{T}^2}\left(2\cos\frac{q_x}{2}+\frac{13}{8}\right)\cos\frac{q_y}{4}\cos\frac{q_z}{4} + \cdots + \frac{s_{\mathbf{q},S=1,10}}{[S(S+1)]^{11}\tilde{T}^{10}}.\end{aligned} \tag{A2}$$

Finally, for $S = \frac{3}{2}$ we have

$$\begin{aligned}\frac{S_{\mathbf{q},S=3/2}}{S(S+1)} = 1 &- \frac{2J}{3\tilde{T}}\left(\cos\frac{q_x}{4}\cos\frac{q_y}{4} + \cos\frac{q_y}{4}\cos\frac{q_z}{4} + \cos\frac{q_x}{4}\cos\frac{q_z}{4}\right)\\ &+ \frac{2J^2}{9\tilde{T}^2}\left(\cos\frac{q_z}{2}\cos\frac{q_x}{2} + \cos\frac{q_y}{2}\cos\frac{q_z}{2} + \cos\frac{q_x}{2}\cos\frac{q_y}{2}\right)\\ &+ \frac{2J^2}{9\tilde{T}^2}\cos\frac{q_x}{4}\cos\frac{q_y}{4}\left(2\cos\frac{q_z}{2}+\frac{9}{5}\right) + \frac{2J^2}{9\tilde{T}^2}\cos\frac{q_x}{4}\left(2\cos\frac{q_y}{2}+\frac{9}{5}\right)\cos\frac{q_z}{4}\\ &+ \frac{2J^2}{9\tilde{T}^2}\left(2\cos\frac{q_x}{2}+\frac{9}{5}\right)\cos\frac{q_y}{4}\cos\frac{q_z}{4} + \cdots + \frac{s_{\mathbf{q},S=3/2,10}}{[S(S+1)]^{11}\tilde{T}^{10}}.\end{aligned} \tag{A3}$$

In the above equations the abbreviation $\tilde{T} = T/[S(S+1)]$ is used. The S dependence of $S_{\mathbf{q}}$ appears first in terms of second order in T. Setting $q_y = 4\pi$ and $q_z = 0$ in these formulas we reproduce the first rows from Table I.

[1] J. S. Gardner, M. J. P. Gingras, and J. E. Greedan, Magnetic pyrochlore oxides, Rev. Mod. Phys. **82**, 53 (2010).

[2] M. J. P. Gingras and P. A. McClarty, Quantum spin ice: a search for gapless quantum spin liquids in pyrochlore magnets, Rep. Prog. Phys. **77**, 056501 (2014).

[3] J. G. Rau and M. J. P. Gingras, Frustrated quantum rare-earth pyrochlores, Annu. Rev. Condens. Matter Phys. **10**, 357 (2019).

[4] S. V. Isakov, K. Gregor, R. Moessner, and S. L. Sondhi, Dipolar Spin Correlations in Classical Pyrochlore Magnets, Phys. Rev. Lett. **93**, 167204 (2004).

[5] C. L. Henley, The Coulomb phase in frustrated systems, Annu. Rev. Condens. Matter Phys. **1**, 179 (2010).

[6] A. B. Harris, A. J. Berlinsky, and C. Bruder, Ordering by quantum fluctuations in a strongly frustrated Heisenberg antiferromagnet, J. Appl. Phys. **69**, 5200 (1991).

[7] M. Isoda and S. Mori, Valence-bond crystal and anisotropic excitation spectrum on 3-dimensionally frustrated pyrochlore, J. Phys. Soc. Jpn. **67**, 4022 (1998).

[8] B. Canals and C. Lacroix, Pyrochlore Antiferromagnet: A Three-Dimensional Quantum Spin Liquid, Phys. Rev. Lett. **80**, 2933 (1998).

[9] B. Canals and C. Lacroix, Quantum spin liquid: The Heisenberg antiferromagnet on the three-dimensional pyrochlore lattice, Phys. Rev. B **61**, 1149 (2000).

[10] A. Koga and N. Kawakami, Frustrated Heisenberg antiferromagnet on the pyrochlore lattice, Phys. Rev. B **63**, 144432 (2001).

[11] H. Tsunetsugu, Antiferromagnetic quantum spins on the pyrochlore lattice, J. Phys. Soc. Jpn. **70**, 640 (2001).

[12] H. Tsunetsugu, Spin-singlet order in a pyrochlore antiferromagnet, Phys. Rev. B **65**, 024415 (2001).

[13] H. Tsunetsugu, Theory of antiferromagnetic Heisenberg spins on a breathing pyrochlore lattice, Progr. Theor. Exp. Phys. **2017**, 033I01 (2017).

[14] E. Berg, E. Altman, and A. Auerbach, Singlet Excitations in Pyrochlore: A Study of Quantum Frustration, Phys. Rev. Lett. **90**, 147204 (2003).

[15] R. Moessner, S. L. Sondhi, and M. O. Goerbig, Quantum dimer models and effective Hamiltonians on the pyrochlore lattice, Phys. Rev. B **73**, 094430 (2006).

[16] O. Tchernyshyov, R. Moessner, and S. L. Sondhi, Flux expulsion and greedy bosons: Frustrated magnets at large N, Europhys. Lett. **73**, 278 (2006).

[17] J. H. Kim and J. H. Han, Chiral spin states in the pyrochlore Heisenberg magnet: Fermionic mean-field theory and variational Monte Carlo calculations, Phys. Rev. B **78**, 180410(R) (2008).

[18] F. J. Burnell, S. Chakravarty, and S. L. Sondhi, Monopole flux state on the pyrochlore lattice, Phys. Rev. B **79**, 144432 (2009).

[19] C. L. Henley, Order by Disorder and Gaugelike Degeneracy in a Quantum Pyrochlore Antiferromagnet, Phys. Rev. Lett. **96**, 047201 (2006).

[20] U. Hizi and C. L. Henley, Effective Hamiltonians for large-S pyrochlore antiferromagnets, J. Phys.: Condens. Matter **19**, 145268 (2007).

[21] U. Hizi and C. L. Henley, Anharmonic ground state selection in the pyrochlore antiferromagnet, Phys. Rev. B **80**, 014407 (2009).

[22] F.-Y. Li and G. Chen, Competing phases and topological excitations of spin-1 pyrochlore antiferromagnets, Phys. Rev. B **98**, 045109 (2018).

[23] V. R. Chandra and J. Sahoo, Spin-1/2 Heisenberg antiferromagnet on the pyrochlore lattice: An exact diagonalization study, Phys. Rev. B **97**, 144407 (2018).

[24] Y. Iqbal, T. Müller, P. Ghosh, M. J. P. Gingras, H. O. Jeschke, S. Rachel, J. Reuther, and R. Thomale, Quantum and classical phases of the pyrochlore Heisenberg model with competing interactions, Phys. Rev. X **9**, 011005 (2019).

[25] S. Zhang, H. J. Changlani, K. W. Plumb, O. Tchernyshyov, and R. Moessner, Dynamical Structure Factor of the Three-Dimensional Quantum Spin Liquid Candidate $NaCaNi_2F_7$, Phys. Rev. Lett. **122**, 167203 (2019).

[26] E. Khatami and M. Rigol, Thermodynamics of the antiferromagnetic Heisenberg model on the checkerboard lattice, Phys. Rev. B **83**, 134431 (2011).

[27] E. Khatami, J. S. Helton, and M. Rigol, Numerical study of the thermodynamics of clinoatacamite, Phys. Rev. B **85**, 064401 (2012).

[28] Y. Huang, K. Chen, Y. Deng, N. Prokof'ev, and B. Svistunov, Spin-Ice State of the Quantum Heisenberg Antiferromagnet on the Pyrochlore Lattice, Phys. Rev. Lett. **116**, 177203 (2016).

[29] J. Kondo and K. Yamaji, Green's-function formalism of the one-dimensional Heisenberg spin system, Prog. Theor. Phys. **47**, 807 (1972).

[30] J. Oitmaa, C. Hamer, and W. Zheng, *Series Expansion Methods for Strongly Interacting Lattice Models* (Cambridge University Press, Cambridge, 2006).

[31] http://lampx.tugraz.at/~hadley/ss1/bzones/fcc.php

[32] J. N. Reimers, A. J. Berlinsky, and A.-C. Shi, Mean-field approach to magnetic ordering in highly frustrated pyrochlores, Phys. Rev. B **43**, 865 (1991).

[33] R. Moessner and J. T. Chalker, Properties of a Classical Spin Liquid: The Heisenberg Pyrochlore Antiferromagnet, Phys. Rev. Lett. **80**, 2929 (1998).

[34] R. Moessner and J. T. Chalker, Low-temperature properties of classical geometrically frustrated antiferromagnets, Phys. Rev. B **58**, 12049 (1998).

[35] J. E. Greedan, M. Sato, X. Yan, and F. S. Razavi, Spin-glass-like behavior in $Y_2Mo_2O_7$, a concentrated, crystalline system with negligible apparent disorder, Solid State Commun. **59**, 895 (1986).

[36] H. J. Silverstein, K. Fritsch, F. Flicker, A. M. Hallas, J. S. Gardner, Y. Qiu, G. Ehlers, A. T. Savici, Z. Yamani, K. A. Ross, B. D. Gaulin, M. J. P. Gingras, J. A. M. Paddison,

K. Foyevtsova, R. Valenti, F. Hawthorne, C. R. Wiebe, and H. D. Zhou, Liquidlike correlations in single-crystalline $Y_2Mo_2O_7$: An unconventional spin glass, Phys. Rev. B **89**, 054433 (2014).

[37] P. M. M. Thygesen, J. A. M. Paddison, R. Zhang, K. A. Beyer, K. W. Chapman, H. Y. Playford, M. G. Tucker, D. A. Keen, M. A. Hayward, and A. L. Goodwin, Orbital Dimer Model for the Spin-Glass State in $Y_2Mo_2O_7$, Phys. Rev. Lett. **118**, 067201 (2017).

[38] S. Gao, K. Guratinder, U. Stuhr, J. S. White, M. Mansson, B. Roessli, T. Fennell, V. Tsurkan, A. Loidl, M. Ciomaga Hatnean, G. Balakrishnan, S. Raymond, L. Chapon, V. O. Garlea, A. T. Savici, A. Cervellino, A. Bombardi, D. Chernyshov, Ch. Rüegg, J. T. Haraldsen, and O. Zaharko, Manifolds of magnetic ordered states and excitations in the almost Heisenberg pyrochlore antiferromagnet $MgCr_2O_4$, Phys. Rev. B **97**, 134430 (2018).

[39] S. Ji, S.-H. Lee, C. Broholm, T. Y. Koo, W. Ratcliff, S.-W. Cheong, and P. Zschack, Spin-Lattice Order in Frustrated $ZnCr_2O_4$, Phys. Rev. Lett. **103**, 037201 (2009).

[40] M. Matsuda, M. Takeda, M. Nakamura, K. Kakurai, A. Oosawa, E. Lelièvre-Berna, J.-H. Chung, H. Ueda, H. Takagi, and S.-H. Lee, Spiral spin structure in the Heisenberg pyrochlore magnet $CdCr_2O_4$, Phys. Rev. B **75**, 104415 (2007).

[41] A. Sadeghi, M. Alaei, F. Shahbazi, and M. J. P. Gingras, Spin Hamiltonian, order out of a Coulomb phase, and pseudocriticality in the frustrated pyrochlore Heisenberg antiferromagnet FeF_3, Phys. Rev. B **91**, 140407(R) (2015).

[42] S. V. Tyablikov, *Methods in the Quantum Theory of Magnetism* (Cambridge University Press, Cambridge, 1967).

[43] W. Gasser, E. Heiner, and K. Elk, *Greensche Funktionen in Festkörper- und Vielteilchenphysik* (Wiley-Blackwell, Weinheim, 2001).

[44] P. Fröbrich and P. J. Kuntz, Many-body Green's function theory of Heisenberg films, Phys. Rep. **432**, 223 (2006).

[45] W. Nolting and A. Ramakanth, *Quantum Theory of Magnetism* (Springer, Berlin, 2009).

[46] H. Shimahara and S. Takada, Green's function theory of the two-dimensional Heisenberg model - spin wave in short range order -, J. Phys. Soc. Jpn. **60**, 2394 (1991).

[47] S. Winterfeldt and D. Ihle, Theory of antiferromagnetic short-range order in the two-dimensional Heisenberg model, Phys. Rev. B **56**, 5535 (1997).

[48] L. Siurakshina, D. Ihle, and R. Hayn, Theory of magnetic order in the three-dimensional spatially anisotropic Heisenberg model, Phys. Rev. B **61**, 14601 (2000).

[49] L. Siurakshina, D. Ihle, and R. Hayn, Magnetic order and finite-temperature properties of the two-dimensional frustrated Heisenberg model, Phys. Rev. B **64**, 104406 (2001).

[50] M. Härtel, J. Richter, D. Ihle, J. Schnack, and S.-L. Drechsler, Thermodynamics of the one-dimensional frustrated Heisenberg ferromagnet with arbitrary spin, Phys. Rev. B **84**, 104411 (2011).

[51] P. Müller, J. Richter, and D. Ihle, Thermodynamics of frustrated ferromagnetic spin-1/2 Heisenberg chains: Role of interchain coupling, Phys. Rev. B **95**, 134407 (2017).

[52] P. Müller, A. Lohmann, J. Richter, O. Menchyshyn, and O. Derzhko, Thermodynamics of the pyrochlore Heisenberg ferromagnet with arbitrary spin S, Phys. Rev. B **96**, 174419 (2017).

[53] W. Yu and S. Feng, Spin-liquid state for two-dimensional Heisenberg antiferromagnets on a kagomé lattice, Eur. Phys. J. B **13**, 265 (2000).

[54] B. H. Bernhard, B. Canals, and C. Lacroix, Green's function approach to the magnetic properties of the kagomé antiferromagnet, Phys. Rev. B **66**, 104424 (2002).

[55] D. Schmalfuß, J. Richter, and D. Ihle, Absence of long-range order in a spin-half Heisenberg antiferromagnet on the stacked kagomé lattice, Phys. Rev. B **70**, 184412 (2004).

[56] D. Schmalfuß, J. Richter, and D. Ihle, Green's function theory of quasi-two-dimensional spin-half Heisenberg ferromagnets: Stacked square versus stacked kagomé lattices, Phys. Rev. B **72**, 224405 (2005).

[57] D. Schmalfuß, R. Darradi, J. Richter, J. Schulenburg, and D. Ihle, Quantum J_1–J_2 Antiferromagnet on a Stacked Square Lattice: Influence of the Interlayer Coupling on the Ground-State Magnetic Ordering, Phys. Rev. Lett. **97**, 157201 (2006).

[58] M. Härtel, J. Richter, D. Ihle, and S.-L. Drechsler, Thermodynamics of a two-dimensional frustrated spin-1/2 Heisenberg ferromagnet, Phys. Rev. B **81**, 174421 (2010).

[59] T. N. Antsygina, M. I. Poltavskaya, I. I. Poltavsky, and K. A. Chishko, Thermodynamics of low-dimensional spin-$\frac{1}{2}$ Heisenberg ferromagnets in an external magnetic field within a Green function formalism, Phys. Rev. B **77**, 024407 (2008).

[60] T. N. Antsygina, M. I. Poltavskaya, I. I. Poltavsky, and K. A. Chishko, Square lattice hard-core bosons within the random phase approximation, Phys. Rev. B **80**, 174511 (2009).

[61] A. V. Mikheyenkov, A. V. Shvartsberg, and A. F. Barabanov, Phase transitions in the 2D $J_1 - J_2$ Heisenberg model with arbitrary signs of exchange interactions, JETP Lett. **98**, 156 (2013).

[62] A. V. Mikheyenkov, A. V. Shvartsberg, V. E. Valiulin, and A. F. Barabanov, Thermodynamic properties of the 2D frustrated Heisenberg model for the entire J_1-J_2 circle, J. Magn. Magn. Mater. **419**, 131 (2016).

[63] A. A. Vladimirov, D. Ihle, and N. M. Plakida, Magnetic susceptibility and short-range order in iron pnictides: Anisotropic $J_1 - J_2$ Heisenberg model, Eur. Phys. J. B **87**, 112 (2014).

[64] A. A. Vladimirov, D. Ihle, and N. M. Plakida, Spin excitations and thermodynamics of the antiferromagnetic Heisenberg model on the layered honeycomb lattice, Eur. Phys. J. B **90**, 48 (2017).

[65] P. Müller, J. Richter, A. Hauser, and D. Ihle, Thermodynamics of the frustrated J_1-J_2 Heisenberg ferromagnet on the body-centered cubic lattice with arbitrary spin, Eur. Phys. J. B **88**, 159 (2015).

[66] P. Müller, A. Zander, and J. Richter, Thermodynamics of the kagome-lattice Heisenberg antiferromagnet with arbitrary spin S, Phys. Rev. B **98**, 024414 (2018).

[67] O. Götze, D. J. J. Farnell, R. F. Bishop, P. H. Y. Li, and J. Richter, Heisenberg antiferromagnet on the kagome lattice with arbitrary spin: A higher-order coupled cluster treatment, Phys. Rev. B **84**, 224428 (2011).

[68] A. Lohmann, H.-J. Schmidt, and J. Richter, Tenth-order high-temperature expansion for the susceptibility and the specific heat of spin-s Heisenberg models with arbitrary exchange patterns: Application to pyrochlore and kagome magnets, Phys. Rev. B **89**, 014415 (2014).

[69] http://www.uni-magdeburg.de/jschulen/HTE/
[70] H.-J. Schmidt, A. Lohmann, and J. Richter, Eighth-order high-temperature expansion for general Heisenberg Hamiltonians, Phys. Rev. B **84**, 104443 (2011).
[71] R. R. Sobral and C. Lacroix, Order by disorder in the pyrochlore antiferromagnets, Solid State Commun. **103**, 407 (1997).
[72] R. Moessner and A. J. Berlinsky, Magnetic Susceptibility of Diluted Pyrochlore and $SrCr_{9-9x}Ga_{3+9x}O_{19}$ Antiferromagnets, Phys. Rev. Lett. **83**, 3293 (1999).
[73] A. J. García-Adeva and D. L. Huber, Classical generalized constant coupling model for geometrically frustrated antiferromagnets, Phys. Rev. B **63**, 140404(R) (2001).
[74] A. J. Garcia-Adeva and D. L. Huber, Classical generalized constant-coupling method for geometrically frustrated magnets: Microscopic formulation and effect of perturbations beyond nearest-neighbor interactions, Phys. Rev. B **65**, 184418 (2002).
[75] K. W. Plumb, H. J. Changlani, A. Scheie, S. Zhang, J. W. Kriza, J. A. Rodriguez-Rivera, Y. Qiu, B. Winn, R. J. Cava, and C. L. Broholm, Continuum of quantum fluctuations in a three-dimensional $S = 1$ Heisenberg magnet, Nat. Phys. **15**, 54 (2019).
[76] N. E. Sherman and R. R. P. Singh, Structure factors of the kagome-lattice Heisenberg antiferromagnets at finite temperatures, Phys. Rev. B **97**, 014423 (2018).
[77] J. C. Halimeh and R. R. P. Singh, Rapid filling of the spin gap with temperature in the Schwinger-boson mean-field theory of the antiferromagnetic Heisenberg kagome model, Phys. Rev. B **99**, 155151 (2019).
[78] H. Yan, R. Pohle, and N. Shannon, Half moons are pinch points with dispersion, Phys. Rev. B **98**, 140402(R) (2018).
[79] P. Müller, *Stark frustrierte Quantenmagnete: Grundzustand und Thermodynamik* (Fakultät für Naturwissenschaften, Otto-von-Guericke-Universität Magdeburg, 2019).
[80] G. Misguich and B. Bernu, Specific heat of the $s = \frac{1}{2}$ Heisenberg model on the kagome lattice: High-temperature series expansion analysis, Phys. Rev. B **71**, 014417 (2005).
[81] T. Munehisa, An improved finite temperature Lanczos method and its application to the spin-1/2 Heisenberg model on the kagome lattice, World J. Condens. Matter Phys. **4**, 134 (2014).
[82] T. Shimokawa and H. Kawamura, Finite-temperature crossover phenomenon in the $S = 1/2$ antiferromagnetic Heisenberg model on the kagome lattice, J. Phys. Soc. Jpn. **85**, 113702 (2016).
[83] A. Baniodeh, N. Magnani, Y. Lan, G. Buth, C. E. Anson, J. Richter, M. Affronte, J. Schnack, and A. K. Powell, High spin cycles: topping the spin record for a single molecule verging on quantum criticality, npj Quantum Mate. **3**, 10 (2018).
[84] J. Schnack, J. Schulenburg, and J. Richter, Magnetism of the $N = 42$ kagome lattice antiferromagnet, Phys. Rev. B **98**, 094423 (2018).